THE GEOLOGICAL SOCIETY
OF AMERICA®

Growth of the southern Tian Shan-Pamir and its impact on central Asian climate

Fabiana Richter[1,7,†], Jozi Pearson[2], Marius Vilkas[2], Richard V. Heermance[2], Carmala N. Garzione[1,3], M. Robinson Cecil[2], Gilby Jepson[4], Annelisa Moe[2], Jianhong Xu[5], Langtao Liu[6], and Jie Chen[5]

[1]*Department of Earth and Environmental Sciences, University of Rochester, Rochester, New York 14620, USA*
[2]*Department of Geological Sciences, California State University Northridge, Northridge, California 911308266, USA*
[3]*College of Sciences, The University of Arizona, 1040 4th St, Tucson, Arizona 85721, USA*
[4]*Department of Geosciences, The University of Arizona, 1040 E 4th Street, Tucson, Arizona 85721, USA*
[5]*State Key Laboratory of Earthquake Dynamics, Institute of Geology, China Earthquake Administration, P.O. Box 9803, Chaoyang District, Beijing 100029, China*
[6]*Department of Prospecting Engineering, Hebei University of Engineering, Handan, Hebei, 056038, China*
[7]*Institute of Geosciences, Instituto Central de Ciências, University of Brasília, Brasília, Federal District, 70297-400, Brazil*

ABSTRACT

Uplift and amalgamation of the high-elevation (>3000 m) Tian Shan and Pamir ranges in Central Asia restricts westerly atmospheric flow and thereby limits moisture delivery to the leeward Taklimakan Desert in the Tarim Basin (<1500 m), the second largest modern sand dune desert on Earth. Although some research suggests that the hyper-arid conditions observed today in the Tarim Basin developed by ca. 25 Ma, stratigraphic evidence suggests the first erg system did not appear until 12.2 Ma. To address this controversy and to understand the tectonic influences on climate in Central Asia, we studied a continuous, 3800-m-thick stratigraphic section deposited from 15.1 to 0.9 Ma now exposed within the western Kepintagh fold-and-thrust belt in the southern Tian Shan foreland. We present new detrital zircon data (n = 839), new carbonate oxygen ($\delta^{18}O_c$) and carbon ($\delta^{13}C_c$) stable isotope compositions (n = 368), structural modeling, and stratigraphic observations, and combine these data with recently published magnetostratigraphy and regional studies to reconstruct the history of deposition, deformation, and climate change in the northwestern Tarim Basin. We find that basins along the southern (this study) and northern (i.e., Ili Basin) margins of the Tian Shan were likely receiving similar westerly precipitation by 15 Ma ($\delta^{18}O_c = {\sim}{-8}$‰) and had similar lacustrine-playa environments at ca. 13.5 Ma, despite differences in sedimentary provenance. At ca. 12 Ma, an erg desert formed adjacent to the southern Tian Shan in the northwestern Tarim Basin, coincident with a mid- to late Miocene phase of deformation and exhumation within both the Pamir and southern Tian Shan. Desertification at ca. 12 Ma was marked by a negative $\delta^{18}O_c$ excursion from -7.8 ± 0.4‰ to -8.7 ± 0.7‰ in the southern Tian Shan foreland (this study), coeval with a negative $\delta^{18}O_c$ excursion (~−11 to −13‰) in the Tajik Basin, west of the Pamir. These data suggest that only after ca. 12 Ma did the Pamir-Tian Shan create a high-elevation barrier that effectively blocked westerly moisture, forming a rain shadow in the northwestern Tarim Basin. After 7 Ma, the southern Tian Shan foreland migrated southward as this region experienced widespread deformation. In our study area, rapid shortening and deformation above two frontal foreland faults initiated between 6.0 and 3.5 Ma resulted in positive $\delta^{13}C_c$ excursions to values close to 0‰, which is interpreted to reflect exhumation in the Tian Shan and recycling of Paleozoic carbonates. Shortening led to isolation of the study site as a piggy-back basin by 3.5 Ma, when the sediment provenance was limited to the exhumed Paleozoic basement rocks of the Kepintagh fold belt. The abrupt sedimentologic and isotopic changes observed in the southern Tian Shan foreland appear to be decoupled from late Cenozoic global climate change and can be explained entirely by local tectonics. This study highlights how tectonics may overprint the more regional and global climate signals in active tectonic settings.

1. INTRODUCTION

Cenozoic aridification of mid-latitude Asia coincided with both gradual global cooling (Zachos et al., 2001; Westerhold et al., 2020) and with the progressive uplift of the Tibetan Plateau and surrounding mountain belts (e.g., Altai, Pamir, Tian Shan). One of the most dramatic examples of Asian aridification is the Tarim Basin (Fig. 1), which was transformed from a relatively wet and warm region containing the Tarim Sea at ca. 34 Ma (Bosboom et al., 2014) into a modern arid endorheic basin that contains the 337,000 km^2 Taklimakan Desert, the second largest erg system on Earth. Desertification of the Tarim Basin (~800–1500 m) has been linked to changes in atmospheric circulation due to growth of the Pamir and Tian Shan mountain belts (>3000 m) that breached westerly winds and partially restricted moisture from reaching the basin (Wang et al., 2017). Whether or not this tectonic-atmospheric framework shifted in the late Oligocene or middle Miocene, however, remains debated (e.g., Wang et al., 2020; Heermance et al., 2018), and the causal relationship between deformation of the Pamir and/or Tian Shan and desert expansion remains poorly understood.

The history of Cenozoic aridification of the Tarim Basin, today occupied by the Taklimakan Desert, initiated with the westward retreat of the easternmost branch of the proto-Paratethys

---

Fabiana Richter https://orcid.org/0000-0001-6990-3679
†fabi.richter@gmail.com.

GSA Bulletin;
published online 21 October 2022

https://doi.org/10.1130/B36471.1; 11 figures; 1 table; 1 supplemental file.

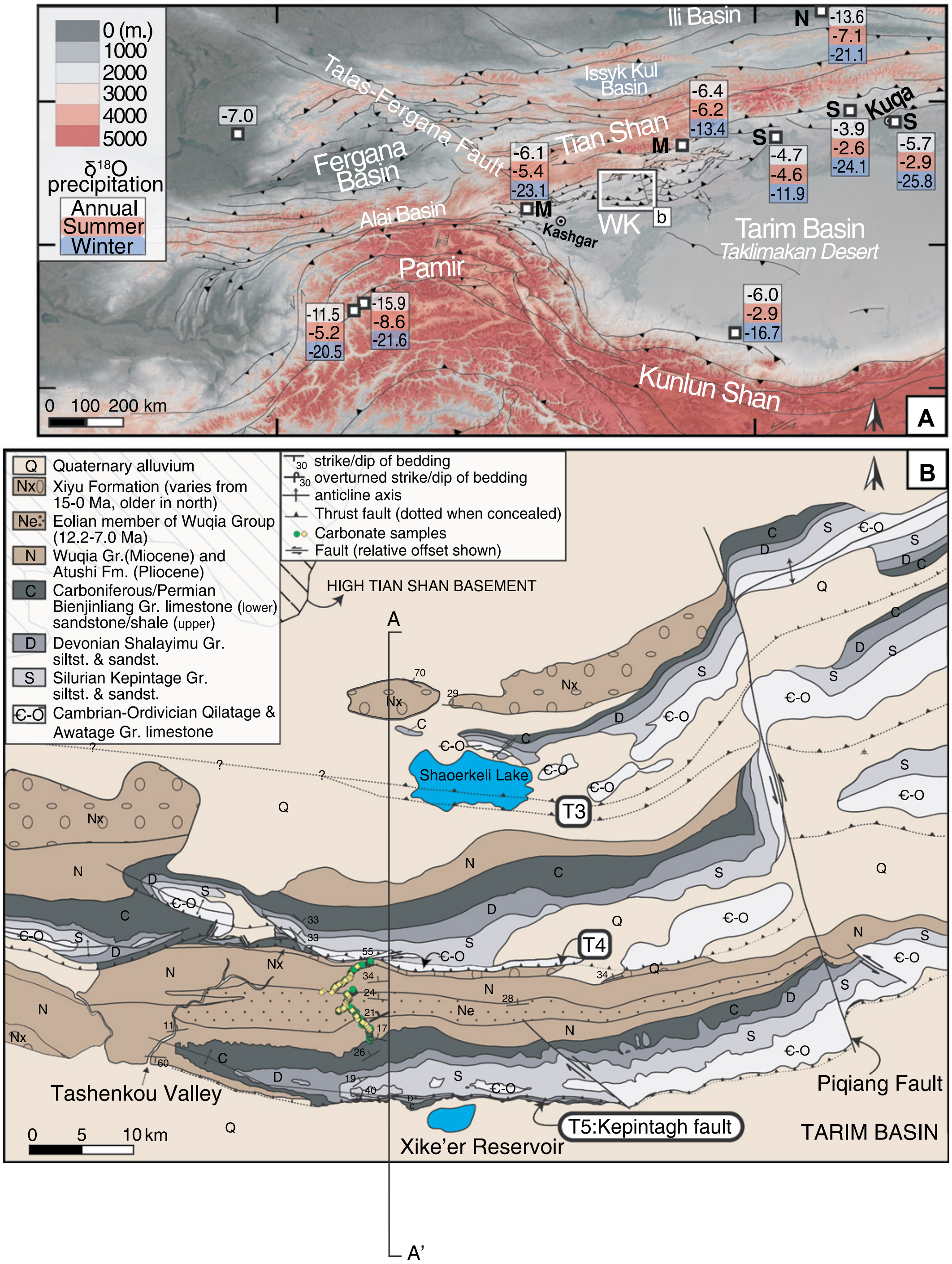

Figure 1. Study area in the West Kepintagh section (WK), northwestern Tarim Basin. (A) Elevation map overlaying satellite imagery indicating main features of the study region and mean precipitation δ^{18}O values (Wang et al., 2016a; Juhlke et al., 2019; IAEA/WMO, 2020). Stations on the Tian Shan region are labeled M (Mountains), N (northern slope), and S (southern slope). (B) Geologic map of the study area. The WK section is marked by the track of samples collected in 2011 (green circles) and 2016 (yellow diamonds). Fm.—Formation; Gr.—Group; siltst.—siltstone; sandst.—sandstone.

Sea, also known as the Tarim Sea, at ca. 34 Ma (Bosboom et al., 2014). Westward retreat of the Tarim Sea at this time resulted from a combination of uplift and deformation related to the Indo-Asian collision and eustatic sea-level lowering associated with global climate cooling (Bosboom et al., 2014). Subsequently, the convergence of the Pamir and the Tian Shan further isolated the Tarim Basin from the Tajik Basin (and Paratethys Sea) to the east. The resulting Pamir-Tian Shan orogen formed a physical barrier along the western boundary of the Tarim Basin that breached the Westerlies (i.e., atmospheric prevailing winds from the west) and restricted moisture transport to the leeward western Tarim Basin (Wang et al., 2017). Recent work suggests this topographic-atmospheric framework was established at ca. 25 Ma, when the Pamir-Tian Shan orogen reached elevations of 3000 m (Wang et al., 2019), leading to significant hydroclimate modifications in Central and East Asia (Caves et al., 2015). Intermittent sand dune deposition is interpreted to have occurred in the Central Tarim Basin from 26.7 to 22.6 Ma (Zheng et al., 2015) based on a few, m-thick eolian sandstone beds interbedded in predominately mudstone units. However, the earliest documented erg-system did not develop until 12.2 Ma, as recorded by a >1000-m-thick stratigraphic section of dune and interdune lithofacies (Heermance et al., 2018). These thick eolian strata are interpreted to represent the ancient Taklimakan Desert and cover an area of at least 240 km^2 in the western Tarim Basin. Similarly, Wang et al. (2014) describe a prevalence of dune deposits within the same strata (upper Wuqia Group) in the Pamir-Tian Shan convergence zone near Ulugqat, Xinjiang, China. Eolian features observed in western Tarim Basin strata at ca. 25 and 12.2 Ma cannot be explained by global climate shifts to more arid conditions. In fact, global Oligo-Miocene climate remained relatively stable until ca. 15 Ma, when it began a continuously cooling trend (e.g., Westerhold et al., 2020). In short, the timing and the underlying cause of desertification remains disputed and has been ascribed to either the Oligocene retreat of the Paratethys Sea, global cooling, and/or development of an orographic rain-shadow on the leeward side of the Pamir and Tian Shan orogens (e.g., Sun et al., 2011; Bosboom et al., 2014; Carrapa et al., 2015; Zheng et al., 2015; Bougeois et al., 2018; Heermance et al., 2018; Li et al., 2022).

The Pamir and Tian Shan orogens have complex tectonic histories related to Cenozoic convergence between India and Eurasia. Pulsed episodes of deformation have been documented at 21–13 Ma, 20–16 Ma, 20–8 Ma, 25–16 Ma, and 6–0 Ma, depending on location (Sobel and Dumitru, 1997; Amidon and Hynek, 2010; Bershaw et al., 2012; Lukens et al., 2012; Thompson et al., 2015; Blayney et al., 2016). Thermochronology, stratigraphy, and structural data from the Tian Shan suggests that Cenozoic uplift initiated at 25–20 Ma (Sobel and Dumitru, 1997; Sobel et al., 2006) and continued during pulsed episodes at ca. 16–13 Ma and after ca. 4 Ma, with the most rapid shortening occurring in Pliocene to recent time (Charreau et al., 2006; Heermance et al., 2008). New thermochronologic data suggests the initiation of faulting occurred as late as 12–11 Ma in the Kepintagh fold-and-thrust belt (Lü et al., 2021). Together, these data sets suggest deformation in the foreland initiated between 25 and 12 Ma, with a pulse of renewed deformation during the Pliocene within the western Tarim Basin.

We hypothesize that although episodes of uplift within the Pamir and/or Tian Shan likely influenced deposition and hydrogeologic conditions locally since the early Miocene, the Pamir-Tian Shan nexus did not form a physical barrier that restricted moisture transport to its leeward slopes (Tarim Basin) until the middle Miocene (ca. 12 Ma), when the ancient Taklimakan Desert formed in the western Tarim Basin (Heermance et al., 2018). Later in the late Miocene-Pleistocene (<6 Ma), the desert migrated southward from its original site and the Tian Shan foreland experienced pulsed Mio-Pliocene deformation. In this manuscript, we evaluate the interplay between local paleoclimate changes and deformation of the Tian Shan foreland between 15 and 1 Ma using multi-parameter, high resolution records from the West Kepintagh (WK) stratigraphic section, where the earliest erg system in the Tarim Basin has been documented (ca. 12.2 Ma; Heermance et al., 2018). The WK section is located within the hanging wall of the Kepintagh thrust fault and comprises strata deposited in the Tian Shan foreland basin in Miocene to Pleistocene time (Fig. 1B). In this manuscript, we present new sedimentological data, oxygen ($\delta^{18}O_c$) and carbon ($\delta^{13}C_c$) stable isotope composition of carbonate samples, U-Pb detrital zircon geochronology, and mapping of the Kepintagh region. A comprehensive analysis of the paleoenvironmental and tectonic evolution of this part of the Tarim Basin is then compared with the structural and isotopic evolution of the Pamir and Tian Shan ranges (Lü et al., 2021; Jepson et al., 2021; Frisch et al., 2019; Macaulay et al., 2016; Sun et al., 2017). Our results suggest desertification and other environmental changes in the western Tarim Basin were the direct result of uplift and deformation of the Tian Shan adjacent to the flexural foreland during the middle and late Miocene. This study implies that broader regional and global climate signals were overprinted by local climatic and environmental changes related to far-field tectonic activity throughout the Miocene and rapid shortening and local uplift since the early Pliocene in the western Tarim Basin foreland.

2. METHODS

2.1. Stratigraphy of the Western Kepintagh Foreland

Field mapping was conducted between 2011 and 2016. Structural measurements were collected from a 60-km-long north-south transect across the western Kepintagh fold-and-thrust belt (A-A', Fig. 1B). A total of 3745 m of Miocene, Pliocene, and Quaternary strata were measured with a Jacob staff and Abney level within the hanging wall of the north-dipping Kepintagh Fault (T5). The thickness of Paleozoic strata (4355 m) was calculated from cross-sections and combined with previously published literature. Total stratigraphic thickness of the combined Paleozoic and Neogene units is 8100 m. The depositional ages of the Neogene strata are 15.1–1.5 Ma, as determined via magnetostratigraphic methods in Heermance et al. (2018; Fig. 2).

2.2. Carbonate Sampling and Stable Isotope Composition Analysis

Carbonate samples (n = 368) from the West Kepintagh section (39.9°N, 77.3°E; Fig. 1) were collected from fluvio-lacustrine-playa (ca. 15–12.2 Ma), eolian dune and interdune (12.2–7 Ma), fluvial floodplain and alluvial fan (7–1 Ma) lithofacies (Figs. 1 and 3). Bulk carbonate samples (n = 301) were collected in 2011 for a paleomagnetic study (but not demagnetized) with an average 8.3 m sample spacing (Fig. 1; Heermance et al., 2018). In 2016, 67 additional carbonate samples were collected from sedimentary rocks interpreted to have been deposited in lacustrine, pedogenic, palustrine, and shallow groundwater settings. Descriptions and interpretations of depositional environments are given in Table S1[1], and field photographs of representative rocks and their interpreted settings are shown in Figure 3.

Carbonate oxygen and carbon isotopic analyses ($\delta^{18}O_c$ and $\delta^{13}C_c$, Vienna Peedee belemnite [VPDB]) were performed in the Stable Isotope Ratios in the Environment, Analytical Laboratory (SIREAL) at the University of Rochester, New York, USA. Carbonate samples were powdered and pretreated with 30% hydrogen peroxide to remove labile organic carbon. Samples were then analyzed for $\delta^{18}O_c$ and $\delta^{13}C_c$ using a ThermoFinnigan Delta (Plus) XP isotope-ratio mass spectrometer in continuous flow mode coupled to a ThermoElectron Finnigan Gasbench. Analytical results are given in Table S1. Standards were run at the beginning of each analytical session and after every set of seven unknown samples. Isotopic measurements were corrected based on the measured values of internal CRAYOLA, PRANG, and THERMO

---

[1] Supplemental Material. Supplemental Methods 1: Structure and Shortening. Supplemental Methods 2: Trishear modeling. Supplemental Data 1: References for compiled thermochronology (AFT) data. Table S1: Carbonate $\delta^{13}C$ (‰VPDB) and $\delta^{18}O$ (‰VPDB) isotopic results and mean values; descriptions of samples and outcrops; interpretations of depositional environments. Table S2: Descriptions, interpreted paleoenvironments and references for locations in Figure 11. Table S3: U-Pb data unknowns. Table S4: U-Pb Temora-2 standard data. Table S5: Statistical analysis of detrital zircon data. Table S6: Location of detrital zircon samples. Please visit https://doi.org/10.1130/GSAB.S.20426853 to access the supplemental material, and contact editing@geosociety.org with any questions.

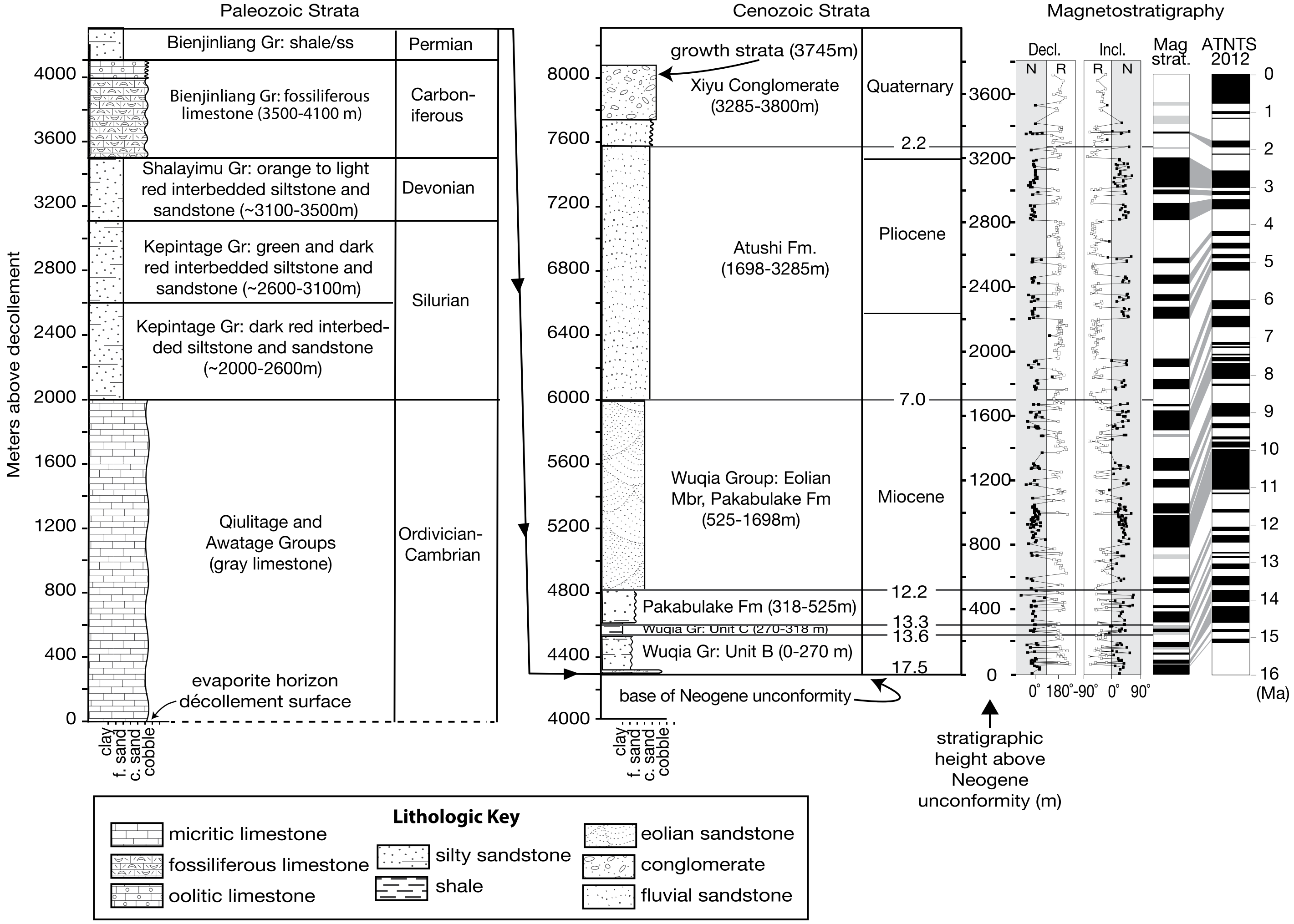

Figure 2. Stratigraphy and magnetostratigraphy of the western Kepintagh belt, northwestern Tarim Basin (Heermance et al., 2007, 2018). Gr.—Group; Fm.—Formation; f.—fine; c.—coarse; Decl.—declination; Incl.—inclination.

CHALK standards. SIREAL internal standards are calibrated using international standards, NBS-18, NBS-19, and L-SVEC. Isotopic permil (‰) values of $\delta^{18}O_c$ and $\delta^{13}C_c$ are reported relative to VPDB.

2.3. U-Pb Detrital Zircon Geochronology

Nine samples were collected from sandstone beds within the WK section, spaced ~300–400 m apart stratigraphically (see Table S6 for sample location coordinates; see footnote 1 for all supplemental tables). Following crushing and pulverizing, standard magnetic and gravimetric heavy mineral separation procedures were used to isolate zircon grains, which were mounted in 2.5 cm epoxy plugs. Zircon mounts were then ground and polished to a 3 μm finish and imaged via backscatter electron (BSE) and cathodoluminescence (CL) detectors on an FEI Quanta 600 scanning electron microscope at California State University, Northridge, California, USA. BSE and CL images were used to guide selection of grains for analysis.

Uranium-lead ratios were collected using a ThermoScientific Element2 inductively coupled plasma–mass spectrometer coupled to a Teledyne Cetec Analyte G2 Excimer Laser (operating at a wavelength of 193 nm). Prior to analysis, the Element2 was tuned using the NIST 612 glass standard to optimize signal intensity and stability. Zircons were ablated using a 25 micron laser beam pulsing at 10 Hz and 80% power. Isotope data were collected in E-scan mode with the magnet set at mass 202, and radio frequency Power at 1245 W. Isotopes measured include ^{202}Hg, ^{204}(Pb + Hg), ^{206}Pb, ^{207}Pb, ^{208}Pb, ^{232}Th, and ^{238}U. Each zircon analysis consisted of a 20 second integration with the laser firing on sample, followed by a 20 second delay to purge the previous sample and move to the next grain. Each ablation pit was drilled to an approximate depth of ~20–30 microns. The primary zircon reference material, 91500 (Wiedenbeck et al., 1995), was analyzed after

Figure 3. Representative photographs of outcrops throughout the 3800 m.-thick West Kepintagh stratigraphic section, northwestern Tarim Basin. Labels in each figure indicate stratigraphic height, age, and sample code. From top-left to bottom-right, photographs indicate rocks and structures that increase in age, as shown by the labels. Sample codes are from carbonates sampled in palustrine, lacustrine, shallow ground water (calcrete) and pedogenic environments. Middle panel on the upper row shows growth strata within the footwall of T4. T4 fault is located ~200 m to the right (north) of outcrop shown in this photo. Fm.—Formation; Mbr.—Member.


Tian Shan limestone
0 cm 1 2 3 4 5 6 7
<5°
20°
50°
Growth Strata
(FOOTWALL OF T4)
1m
Atushi Fm.
Calcrete (shallow groundwater)
3.9 Ma
2713 m.
16KN22c
Atushi Fm.
Calcrete (shallow groundwater)
4.2 Ma
2585 m.
16KN29c
Atushi Fm.
Fluvial
Palustrine (floodplain)
5.1 Ma
2242 m.
16KN67c
Atushi Fm.
Fluvial
Palustrine (floodplain)
Fluvial
6.9 Ma
1730 m.
16KN60c
Pakabulake Fm.
Eolian Mbr.
7.2 Ma
1673 m.
16KN17c
Eolian
Interdune paleosol
Pakabulake Fm.
Eolian Mbr.
Interdune palustrine
Eolian
7.9 Ma
1550 m.
16KN15c
Pakabulake Fm.
Eolian Mbr.
Eolian
Interdune lacustrine
8.4 Ma
1460 m.
16KN13c
Pakabulake Fm.
Eolian Mbr.
Eolian
Interdune palustrine
Eolian
8.6 Ma
1410 m.
16KN11c
Pakabulake Fm.
Eolian Mbr.
Interdune palustrine
Eolian
9.5 Ma
1115 m.
16KN05c
Pakabulake Fm.
Eolian Mbr.
Eolian
Interdune palustrine
10.5 Ma
230 m.
16KN56c
Pakabulake Fm.
Eolian Mbr.
Interdune paleosol
Eolian
11.5 Ma
703 m.
16KN52c
Unit C
Lacustrine
13.4 Ma
294.5 m.
16KN46c
Pakabulake Fm.
Fluvial
Paleosol
13.7 Ma
230 m.
16KN44c

every 10 unknowns to correct for in-run fractionation of Pb/U and Pb isotopes. A second zircon standard, Temora-2, was also analyzed every 10 analyses to assess accuracy and reproducibility of the data. Total uncertainties (analytical + systematic) were determined using the Iolite v4 software package. U-Pb analysis of Temora-2 during all analytical sessions yielded concordant results and error-weighted average age of 416.4 ± 1.7 Ma ($n = 109$), which closely agrees with the accepted ages of 416.8 ± 1.3 Ma and 418.4 ± 6.6 Ma (Black et al., 2004; Mattinson, 2010). U-Pb isotopic data were plotted using IsoplotR 4.4 (Vermeesch, 2018). Corrections for minor amounts of common Pb in zircon were made following methods of Tera and Wasserburg (1972) using measured $^{207}Pb/^{206}Pb$ and $^{238}U/^{206}Pb$ ratios and an age-appropriate Pb isotopic composition of Stacey and Kramers (1975). Concordance was calculated using the log ratio distance from concordia method of Vermeesch (2021) and a 20% discordance filter was applied to all U-Pb dates. A total of 893 zircon U-Pb dates (~95 per sample) remained after filtering and are used in interpretation of the WK strata. U-Pb age data for unknown zircons and for the Temora-2 standard can be found in Tables S3 and S4, respectively.

2.4. Cross-Section, Structural Geology

Structural data were collected and a cross-section was constructed across a 60-km-long north-south transect of the western Kepintagh fold-and-thrust belt (Fig. 1B). Cross-section balancing was completed using FaultFold Version 6.2.0 software from Dr. R. Allmendinger at Cornell University (https://www.rickallmendinger.net/faultfold). This program creates balanced cross-sections based on dip data of the fault plane, or dip data of strata above the fault plane, and can account for trishear fold geometries (Allmendinger, 1998). Values used for fault dip, trishear angle, and propagation-to-slip ratio (P/S) ratio of the three studied structures (T3, T4, T5) are defined in Supplemental Methods 2 (see footnote 1). Line length shortening estimates were then determined for strata above the basal décollement, interpreted to exist within the evaporite horizon near the base of the Cambrian carbonate section (Qiulitage Group, Figs. 1 and 4). Length of shortening is determined by the equation:

$$\Delta l = |l_{\text{final}} - l_{\text{initial}}| \tag{1}$$

where Δl is the change in length, l_{final} is post-deformation length, and l_{initial} is pre-deformation length.

Maximum and minimum shortening rates were calculated for each individual structure as well as for the total cross-section (T3 + T4 + T5) and the two southern folds (T4 + T5) (Table 1). The maximum and minimum shortening rates are based on the Δl and the maximum age determinations defined in section 4.1 (Table 1). The minimum shortening rate is calculated from the equation

$$\Delta l/(\textit{max age \#1}) \tag{2}$$

where *max age #1* is the oldest age for the initiation of deformation based on geologic arguments described in the text. Maximum shortening rate is calculated as

$$\Delta l/(\textit{max age \#2}) \tag{3}$$

where *max age #2* is the youngest age for the initiation of deformation across the structure or structures.

3. RESULTS

3.1. Sedimentology

3.1.1. Paleozoic Stratigraphy

Up to 4300 m of Paleozoic strata are exposed in the western Kepintagh thrust belt (Figs. 1

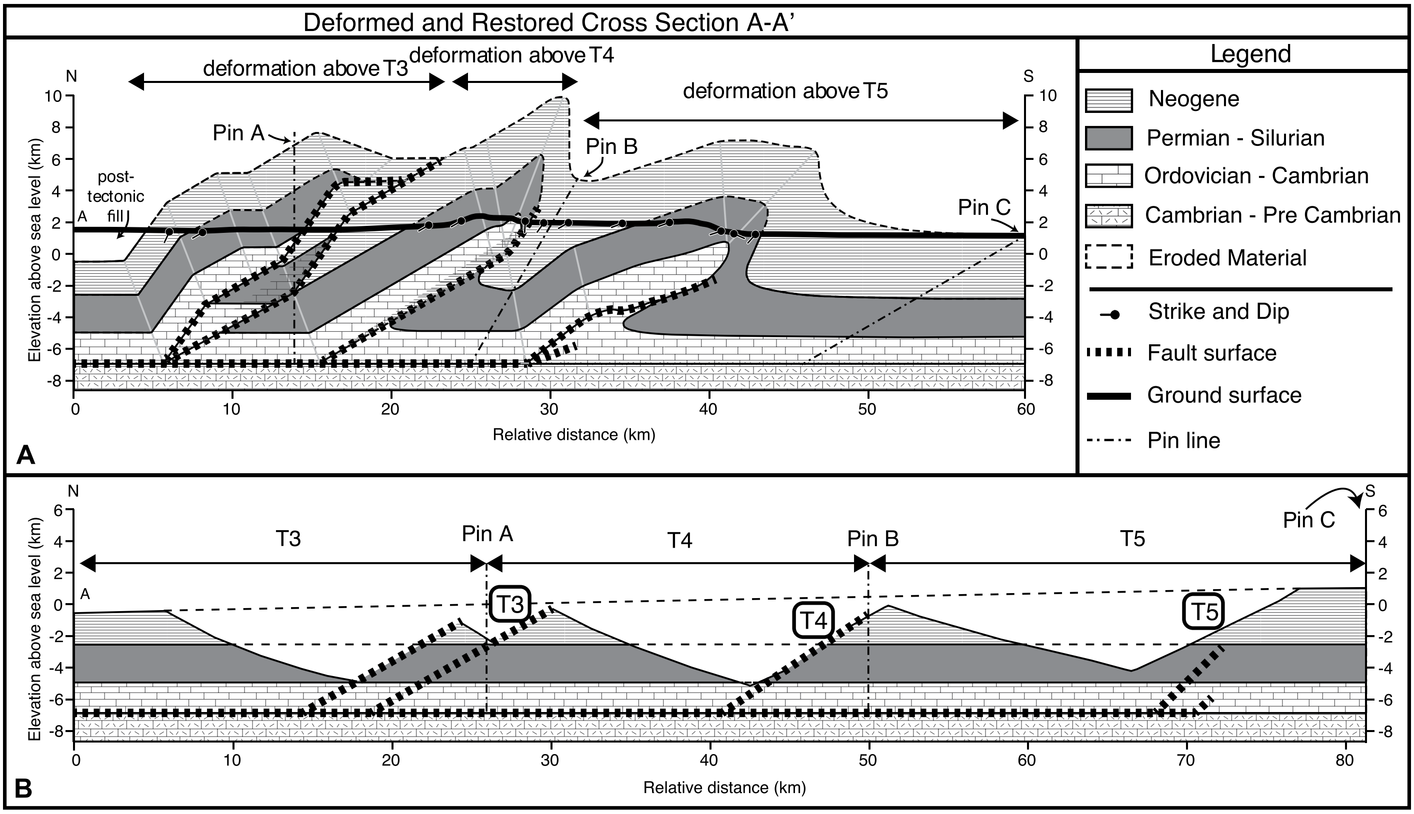

Figure 4. Cross-section and retrodeformed cross section across the study area shown in Figure 1, in the northwestern Tarim Basin.

TABLE 1. SHORTENING AND SHORTENING RATE CALCULATIONS FOR INDIVIDUAL FOLDS AND FOLD AGES IN WESTERN KEPINTAGH FOLD-AND-THRUST BELT, NORTHWESTERN TARIM BASIN

Location	Shortening (km)	Shortening error (km)	Max age #1 (Ma)	Max age #2 (Ma)	Min age (Ma)	Minimum rate (mm/yr)	Maximum rate (mm/yr)
T3	11.9	1.2	12	na	0	0.99	na
T4	12.9	1.3	6	3.5	0	2.2	3.7
T5	10.5	1.1	6	3.5	0	1.8	3.0
T4 + T5	23.4	2.4	6	3.5	0	3.9	6.7
T3 + T4 + T5	35.3	3.5	12	na	0	2.9	na

Notes: na—not applicable. Maximum ages described in text.

and 2). All Paleozoic ages are from previously published studies (e.g., McKnight, 1993; Allen et al., 1999; Turner et al., 2010; Chang et al., 2019). The oldest strata preserved in the foreland are the Cambrian to Ordovician Qiulitage and Awatage groups and consist of massive gray carbonate with a salt or gypsum layer at the base that acts as the décollement within the field area (e.g., Turner et al., 2010; Yang et al., 2018; Chang et al., 2019; Zhang et al., 2019). Above the Ordovician carbonate are ~1100 m of Silurian Kepintagh Group strata; the lower half consisting of dark-red siltstone and sandstone, and the upper half interbedded green and red siltstone and sandstone beds. ~400 m of the Devonian Shalayimu Group is above the Kepintagh Groups strata, and consist of prominent orange and pink siltstone and sandstone. Strata of the Bienjinliang Group overlie the Shalayimu Group, and consist of resistant fossiliferous limestone and red and green siltstones and sandstones, followed by ~500 m of fossiliferous limestone, ~100 m of oolitic limestone, then ~200 m of interbedded siltstones and sandstones that are Carboniferous in age.

3.1.2. Neogene Stratigraphy

Five stratigraphic units comprise the 3800 m section of Neogene strata. Sedimentary terminology and fluvio-lacustrine interpretations follow those defined for the Kashgar Basin, located ~100 km west of the WK, after Heermance et al. (2007) (Figs. 2 and 5). The base of the section is marked by a 1 m thick sedimentary breccia above a disconformity with Paleozoic strata. Above this contact, 270 m of laminated and massive dark red, beige, and brown mudstone define Wuqia Group Unit B, interpreted as fluvial overbank, floodplain, and meandering river

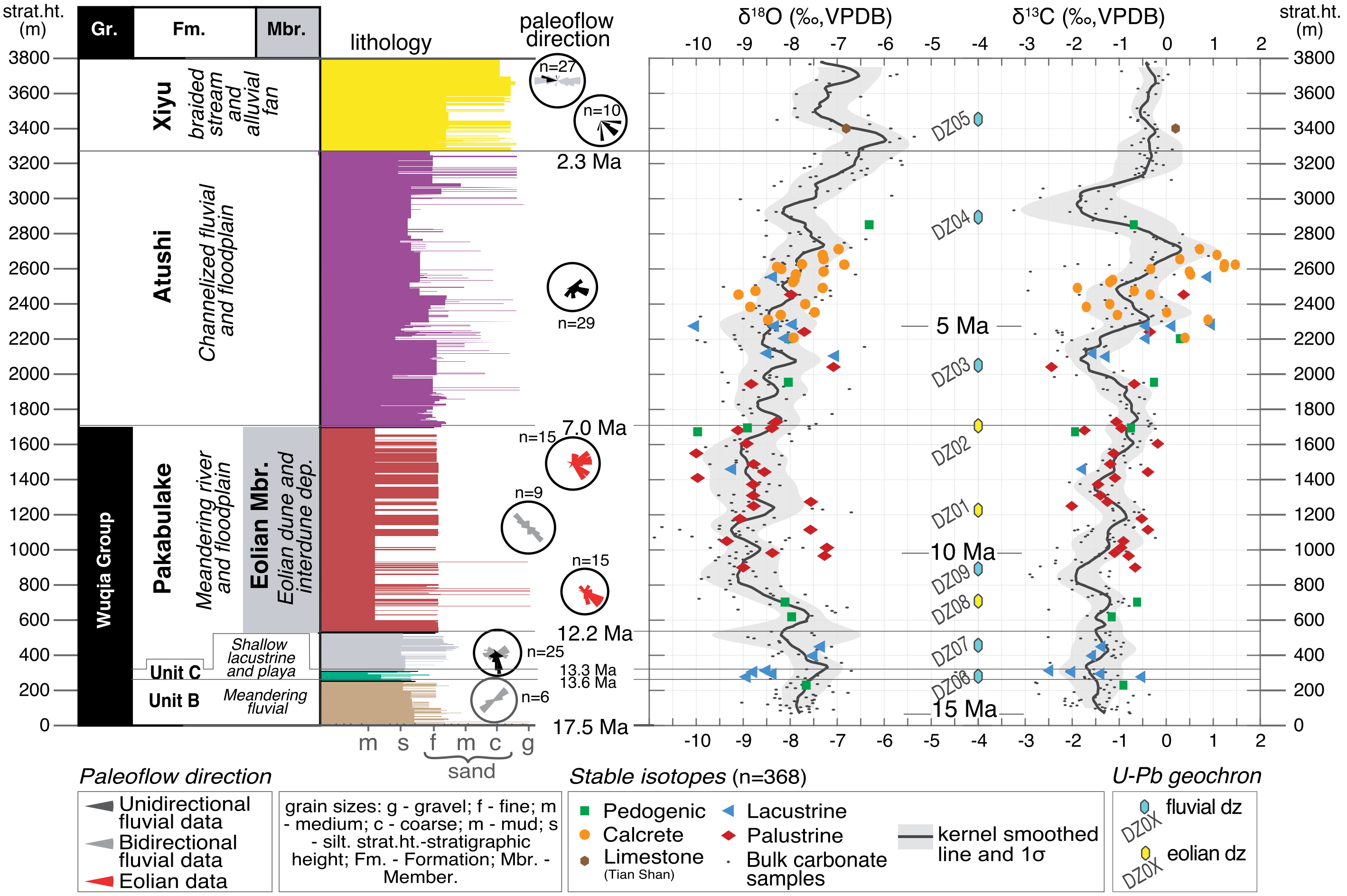

Figure 5. Stratigraphic height in the WK section versus $\delta^{18}O_c$ and $\delta^{13}C_c$ values. Stratigraphy and paleoflow directions are from Heermance et al. (2018). Smoothed $\delta^{18}O_c$ and $\delta^{13}C_c$ lines include all samples and 68% confidence intervals are shown. Gr.—Group; VPDB—Vienna PeeDee belemnite; dep.—deposit; dz—detrital zircon.

deposition. A few intervals show 30–55-cm-thick, massive, brown-red, mottled mudstones showing spheroidal weathering, interpreted as paleosols. These strata were deposited between 15.1 and 13.6 Ma, although the age for the base of the section is poorly constrained by the magnetostratigraphy. Paleochannel margins suggest SW-NE paleoflow.

The stratigraphy changes dramatically from 270 to 318 m (13.6–13.3 Ma). Strata change to interbedded red and green shales that are continuous, planar, gypsiferous, and carbonate- and clay-rich (Fig. 2 and 3). These beds define Wuqia Group Unit C that represents shallow lacustrine and playa deposition. Correlative strata are observed 100 km to the west, north of Kashgar City (Fig. 1A).

Between 318 and 525 m (13.3–12.2 Ma), tabular and lenticular beds of yellow-brown sandstone contain abundant ripples and cross-strata and are interbedded with gray to reddish-brown calcareous mudstone. These beds comprise the lower Pakabulake Formation of the Wuqia Group and represent meandering river channels, overbank deposits, and intermittent lake deposition at ~397 m and ~449 m. Ripple and trough cross-stratification are consistent with east-west flowing paleovalleys. Between 525 and 1698 m (12.2–7.0 Ma), the stratigraphy again changes to well-sorted, pale-red, fine-grained sandstone characterized by >1-m-thick, planar, continuous beds with meter-scale cross-bedding (Fig. 2 and 3) interbedded with massive and crudely laminated mudstone. Sand grains are well-sorted, rounded and show evidence of pits, depressions and upturned plates (see fig. 3b in Heermance et al., 2018). Sandstone beds contain 0.2–1.5 m amplitude tabular cross-bedding and have 1–3 mm, upward-coarsening laminations. These strata have been described by Heermance et al. (2018) and are interpreted as eolian dune and interdune deposits that represent the oldest record of the Taklimakan Desert. These strata are part of a newly defined unit called the Eolian Member in the upper Pakabulake Formation (Heermance et al., 2018). Meter-scale, unidirectional cross-beds dip east-southeast, implying westerly winds (paleoflow directions in Fig. 5). Laminated and massive brown mudstone intervals within the sand-dune lithofacies are interpreted as fluvial and palustrine interdune deposits and are interpreted to have formed in damp interdune settings where carbonate-rich, red-brown, laminated and massive, clay-dominated mudstone were deposited (at 900 m, 966 m, 983 m, 1013 m, 1050 m, 115 m, 1178 m, 1250 m, 1274 m, 1310 m, 1373 m, 1410 m, 1444 m, 1489 m, 1550 m, 1605 m, 1681 m, 1693 m). Ongoing dune migration accompanied by water table rise is commonly associated with interdune ponds, floodplain and overbank muds subjected to intermittent desiccation and pedogenic modification (Mountney, 2012). Beds that show well-developed pedogenesis, with bioturbation in clay-dominated massive mudstone, spheroidal and blocky weathering, mottling and reduction in root traces (at 619 m, 703 m, 1673 m, and 1695 m) are interpreted as interdune paleosols. One interval showing green-yellow, laminated, organic-rich lime mudstone (at 1460 m) is interpreted as a shallow interdune lake.

From 1698 to 3285 m (7.0–2.2 Ma), siltstone and fine sandstone lenses are interbedded with m-thick medium sandstone beds that pinch out laterally over ~100 m and contain epsilon cross-beds. These strata comprise the Atushi Formation and are interpreted as channelized sands within fluvial sheet flow and floodplain deposits. Mudstone beds are massive to laminated, light-brown to red-brown and very calcareous. Intervals consisting of 1–5 m thick, laminated, gray lime claystone and siltstone, with spheroidal weathering and without bioturbation (at 2102 m, 2120 m, 2205 m) are interpreted to have been deposited in shallow lacustrine environments. Intervals with 40–60-cm-thick massive and very calcareous siltstone and claystone with local weak laminations, spheroidal weathering, and weak pedogenesis (i.e., 1730 m, 1945 m, 2042 m, 2242 m) are interpreted to have been deposited in palustrine environments (ponds and floodplain deposits). Clay-rich, massive, mottled, very calcareous and bioturbated ~60-cm-thick beds (at 1955 m, 2203 m) are interpreted to represent paleosols. Continuous fine-sandstone layers are interpreted to have formed by sheet-wash deposition in a floodplain, while medium-grained, discontinuous, cross-bedded sandstone beds are interpreted to have been deposited in fluvial channels. Toward the top of the Atushi Formation (above 2208 m), sandstone interbedded with calcrete dominate. Calcrete consists of silty material heavily cemented by carbonate, forming beds that are mostly massive, discontinuous, lenticular, <10-cm-thick, and light gray-beige-white (at 2208 m, 2311 m, 2338 m, 2353 m, 2384 m, 2400 m, 2454 m, 2475 m, 2492 m, 2526 m, 2538 m, 2569 m, 2585 m, 2600 m, 2611 m, 2625 m, 2627 m, 2656 m, 2680 m, 2713 m). Calcrete texture and sedimentary structures are interpreted to reflect carbonate precipitation in the capillary fringe zone near the water table surface from shallow ground water. The uppermost part of the section (3285–3800 m) consists of coarse-grained, carbonate-cemented sandstone, and cobble and pebble conglomerate that characterize the Xiyu Formation, and represent braided stream and alluvial/delta fan deposition.

3.2. Structural Deformation in the Study Area

At the longitude of the study area, the Kepintagh fold-and-thrust belt consists of three, imbricate, E-W–trending thrust faults spaced ~15 km apart (Fig. 1B). From north to south, these faults were named T3, T4, and T5 by Lü et al. (2021), as indicated in Figures 1 and 4. The Southern Tian Shan Fault System is exposed in the Tian Shan basement ~70 km north of our study area and was not described here. Detailed structural mapping along a N-S cross-section defines the structural style within this part of the fold-and-thrust belt. Here we describe the structure from north-to-south.

The northernmost imbricate fault (T3) within the foreland in our cross section exhumes Late Carboniferous carbonate in the hanging wall north of Shaoerkeli Lake (Fig. 1B). The fault is exposed to the east of our section (Turner et al., 2010) but is concealed in lacustrine sediments in our study area. Beds in the hanging wall of T3 dip 30–70° north. The change in dip defines a hinge line and implies that one fault surface was translated over an underlying fault surface, thus doubling the dip angle on the fault surface.

Approximately 15 km south of the concealed trace of T3, T4 extends E-W for at least 70 km and juxtaposes Cambrian and Ordovician carbonate with the Quaternary Xiyu Conglomerate (Fig. 1). The fault zone contains a 1-m-thick gouge, multiple discrete fault planes, and a 10-m-thick brecciated fault zone. The hanging wall comprises a south vergent anticline with a north limb dipping 30° and a vertical to overturned south limb. Cross-section modeling suggests this structure is a fault propagation fold above a fault ramp dipping 30° N. We interpret the fault ramp to flatten into evaporite horizons at the base of the Cambrian-Ordovician carbonate unit.

The southernmost fault T5, also called the Kepintagh fault, contains a south-vergent anticline in its hanging wall with a 10–40° dipping north flank and a south flank overturned 70°. The anticline exposes Cambrian carbonate in its core. The fault comprises a wide (>10 m) fault zone and extends for at least 70 km from the Piqiang fault to Tashenkou River Valley and is likely a blind thrust to the west of the Tashenkou Valley based on surface structures (Fig. 1).

3.2.1. Cross-Section

A 60-km-long structural cross-section (A-A’) was drawn across the three main structures (T3–T5) and through the study area (Figs. 1B and 4). For our cross-section reconstruction, the décollement depth was fixed at ~7 km below sea level at the base of the Cambrian Qiulitage Group. This depth is consistent with cross-sections by

Allen et al. (1999) and Turner et al. (2010) across the Kepintagh foreland. Moreover, the Cambrian carbonate is the deepest part of the Paleozoic section exposed in the hanging wall of T4 and T5, and suggests that the décollement must be deeper than the deepest-exposed strata.

The northernmost structure T3 is best modeled as a fault-bend fold above two faults in the subsurface. This geometry is interpreted as a duplex structure in the subsurface based on two main observations: (1) dip data on the back limb of the exposed structure that can be reconciled by the presence of an additional ramp in the subsurface, and (2) two structures that are evident at the surface east of the Piqiang fault are interpreted to be concealed within Quaternary sediments in the study area. Surface dip data do not allow the subsurface to be resolved with a simple fault-propagation structure because the lowest part of the hanging-wall stratigraphy (Cambrian carbonate) is not exposed, and there is no evidence of an asymmetrical structure or overturned forelimbs, as is the case with the T5 and T4 structures further south. Total shortening across T3 is 11.9 ± 1.2 km, and (U-Th)/He thermochronology from the hanging wall of T3 suggests initial exhumation occurred at 11–12 Ma (Lü et al., 2021). Thus, we use 12 Ma as the maximum age for initiation of this structure.

Exposed Paleozoic strata near both the T4 and T5 fault zones thins approaching the fault, and these zones are best modeled as trishear folds above emergent fault tips. Trishear modeling is described in detail in Supplemental Methods 2 but can be summarized as a modification of a fault propagation fold above an emergent fault tip. An additional structure appears to exist in the subsurface beneath T5, based on the increasing dip angle of bedding (10° increasing to 60°) from south to north in the hanging wall along the north fold limb. This increase in dip can be resolved by either folding of the northern limb or by the formation of a new fault structure in the subsurface. The steeper dips to the north, however, are incompatible with any models of south-vergent trishear folding, and thus we interpret a second structure must be present in the subsurface. This nascent structure has little slip on the fault surface as evident by the small amount of surface expression seen in the surface dip data. Total shortening magnitudes are 12.9 ± 1.3 km for T4 and 10.5 ± 1.1 km for T5 (Table 1). The age for initiation of the T4 and T5 is inferred to be between 6.0 and 3.5 Ma, based on magnetostratigraphy combined with detrital zircon data, as described in section 4.1 (see discussion section 4.1 below). Total shortening across the two southern structures (T4 + T5) is 23.4 ± 24 km and across all threefolds (T3 + T4 + T5) is 35.3 ± 3.5 km.

3.2.2. Growth Strata

Growth Strata were observed at the top of the Xiyu Conglomerate, adjacent to the T4 emergent fault tip and within the back limb of the T5 structure (Fig. 3). These strata formed within the Xiyu Conglomerate and are characterized by rapidly shallowing dips and angular unconformities within the upper ~100 m of the stratigraphic section. As a fold grows over time, the dips along the fold flanks may steepen. When strata are subaerial, new deposition on these deformed fold flanks will create a buttress unconformity (or angular unconformity if erosion has occurred). With time, growth strata can be buried, exposed, or eroded (Vergés et al., 2002). Although we cannot be sure whether older growth strata were eroded in this section, the preserved growth strata unambiguously define syn-tectonic deposition above the underlying T5 fault ramp. Magnetostratigraphy from Heermance et al. (2018; Fig. 2) places the development of these growth strata at 0.9 Ma. Thus, T5 must have been active by 0.9 Ma and continues to be active today.

3.3. U-Pb Detrital Zircon (DZ) Data

U-Pb analytical results are shown in Tables S3 and S4. Of the nine samples collected for DZ analysis, six are from sandstones interpreted as fluvial in origin (DZ03, DZ04, DZ05, DZ06, DZ07, DZ09) and three are from beds interpreted as eolian dune deposits (DZ01, DZ02, DZ08; Fig. 6). The stratigraphic heights above the Paleozoic strata where samples were collected are shown in Figure 5. Detrital zircon spectra from all samples are complex, with multiple populations ranging in age from Archean (ca. 2.5 Ga) to Triassic (214 Ma) (Fig. 6). Only one sample, DZ08 from near the base of the eolian member of the Pakabulake Formation, yielded young (Miocene) grains that approach the depositional age of the strata. These might be linked to Miocene magmatism in the Pamir dated at ca. 11 Ma (Ducea et al., 2003). Although all samples yielded a smattering of Precambrian ages, pre-Neoproterozoic dates rarely define discernible age peaks. In contrast, populations with age peaks between 840 and 740 Ma are common in all DZ spectra (Fig. 6). In all samples, complexly distributed Phanerozoic ages make up 30%–65% of dated grains. Age peaks vary between samples, but most have multiple populations in Ordovician-Silurian, as well as Permian time. Three of the samples analyzed also yielded Late Triassic populations, with age peaks between 236 and 213 Ma. In order to link the detrital zircon signal with specific source-regions, we compiled the results from recent U-Pb studies within western Tarim river catchments as shown in Figure 7. Because of the complexity of the DZ spectra from the study section, statistical analysis was also used to assess similarities and differences between samples and between samples and compiled data (Fig. 7). Results of that statistical analysis are given in Table S5 and expressed graphically in the multidimensional scaling (MDS) plot of Figure 8. The lowermost sample (DZ06), collected from the Wuqia Group, is statistically similar to the uppermost sample from the Xiyu Formation (DZ05). Samples collected from the Pakabulake and lower Atushi formations (DZ07, DZ09, and DZ03) are all very similar to one another (cross-correlation and likeness >0.7, similarity values >0.9; Table S5). The sample from the upper Atushi Formation (DZ04) is dissimilar to all others. Eolian samples are considered separately, given the different nature of the derivation of grains in those beds, but they are generally most similar to the Wuqia and Xiyu samples (Fig. 8).

3.4. Carbonate Oxygen and Carbon Stable Isotopes

Carbonate samples (n = 368) from the WK section, spanning 15–1 Ma, were collected from fluvio-lacustrine-playa (ca. 15–12.2 Ma), eolian dune and interdune (12.2–7 Ma), and fluvial floodplain and alluvial fan (7–1 Ma) deposits (Figs. 3 and 5). Of these, 67 samples were collected from selected strata deposited in lacustrine, pedogenic, palustrine, and shallow groundwater environments. The additional 301 samples, referred to hereafter as bulk carbonate samples, represent carbonate-rich mudstones and sandstones that were collected originally for paleomagnetic analysis. Isotopic values are shown in Figure 5 (versus thickness) and Figure 9 (versus age). In both figures, we present smoothed curves obtained using an Epanechnikov kernel line smoothing method (Sherfey et al., 2018) based on $\delta^{13}C_c$ and $\delta^{18}O_c$ values of all samples (thickness bandwidth of 67 m equivalent to an age bandwidth of 250 k.y.).

From 15 to 1.1 Ma, $\delta^{18}O_c$ values ranged from −10.9 to −4.3‰, with an average value of −8.1 ± 1.0‰, and $\delta^{13}C_c$ values ranged from −3.2 to –1.5‰, with an average value of −1.0 ± 0.8‰. Overall, from 15 to 1.1 Ma, $\delta^{13}C_c$ mean values increased by ~1‰, but significant swings in mean values (up to 4.5‰) are observed from ca. 6–2.8 Ma, during the transition between channelized fluvial and floodplain to alluvial fan deposition (upper Atushi Formation), and relatively constant values (−0.5 ± 0.5‰) are observed from 2.8 to 1.1 Ma, when alluvial fan deposits dominated. $\delta^{13}C_c$ values peak around 0‰ at ca. 5 Ma, 4 Ma, and after 3 Ma, which are similar to values measured in angular limestone pebbles ($\delta^{13}C_c = 0.2$, $\delta^{18}O_c = 6.8‰$)

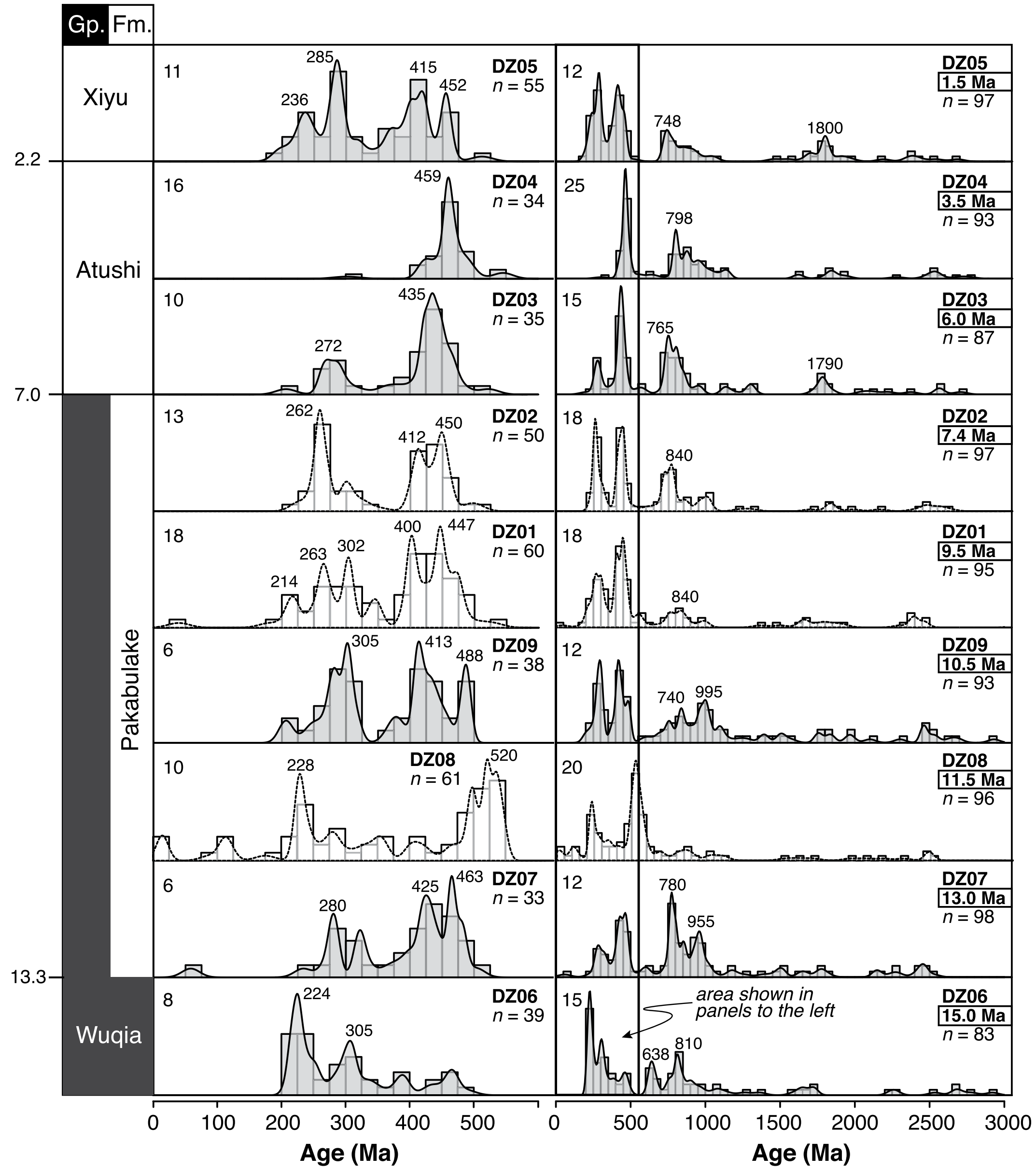

Figure 6. Kernel density estimation plots of detrital zircon ages from each sample collected from the West Kepintagh stratigraphic section in the northwestern Tarim Basin. Histogram bin width is 25 Ma for the Phanerozoic ages (left side panels), and 50 Ma for the entire age spectra (right side panels). Numbers in the upper left of each panel are the maximum heights of the histogram bars. Depositional ages inferred from magnetostratigraphy (Heermance et al., 2008) are given in the boxes on the right side panels. Fm.—Formation; Gp.—Group.

(Fig. 3) collected from a modern stream draining from the Tian Shan (plotted at the stratigraphic height they were collected; Fig. 5). Overall, $\delta^{18}O_c$ values are most positive in the oldest (ca. 15–12 Ma) and youngest (ca. 4–1 Ma) parts of the section, whereas more negative values occur between 11.5 and 7 Ma. The lowest mean values of ~–8.7 ± 0.7‰ occur from 12 to 7 Ma when dune and interdune environments predominated.

The isotopic composition of carbonate is related to specific processes within any particular depositional environment. We therefore subdivide a portion of our samples by paleoenvironment to identify any isotopic excursion related to external climate forcing. Figures 5 and 9 show the $\delta^{18}O_c$ and $\delta^{13}C_c$ of interpreted lacustrine, palustrine, pedogenic, shallow groundwater carbonates, and carbonate cement (Table S1). Paleolacustrine deposits are characterized by laminated or massive calcareous mudstone, with colors varying between gray, green, and brown. $\delta^{18}O_{lacustrine}$ values increase by ~1‰ right before 12.2 Ma, when sand dunes first appeared in this part of the Taklimakan Desert (Heermance et al., 2018), to ~–7.4‰, higher than the value of −9.2‰ in an interdune lake at ca. 8.4 Ma. From ca. 5.5–4 Ma, in the middle Atushi Formation, $\delta^{13}C_{lacustrine}$ show a significant increase of up to 2.5‰ to mean values around 0‰. Pedogenic deposits are represented by massive tan-brown to reddish brown mudstone, locally mottled and bioturbated. $\delta^{18}O_{pedogenic}$ from these strata have similar values before and in the early stages of desert formation (13.6–11.5 Ma), and these values are up to 1.5‰ higher than pedogenic carbonate in later stages of the desert in this region (ca. 7 Ma). $\delta^{13}C_{pedogenic}$ values remain relatively constant throughout the record at −0.8‰ with a mean absolute deviation of 0.4‰. Palustrine deposits are laminated and massive tan-to-reddish mudstone that show varying degrees of pedogenic modification, including mottling and bioturbation, and often show spheroidal weathering. Desiccation cracks are observed in the upper part of some beds. Palustrine carbonates are mostly found in interdune settings from 10.5 to 7 Ma, where the mean $\delta^{18}O_{palustrine}$ value is −8.6 ± 0.8‰. Non-pedogenic carbonate layers occur as 2–10-cm-thick white-gray, massive, discontinuous lenses within siltstone and sandstone rocks, and calcretes associated with

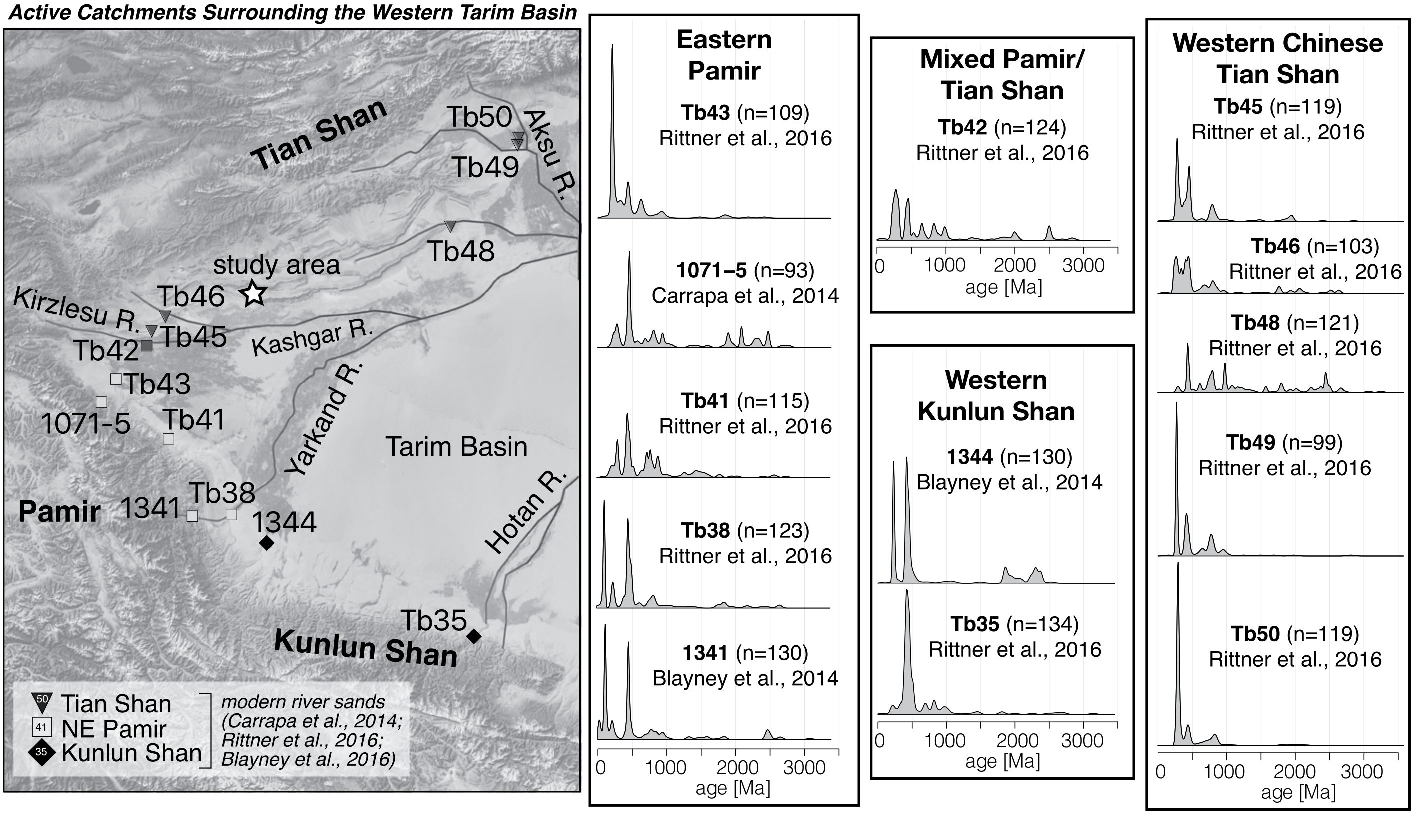

Figure 7. Location of modern river sand samples collected from fluvial catchments in the Pamir, Tian Shan, and Kunlun (previous studies listed on bottom left) and corresponding kernel density estimate plots for each location. R.—River.

carbonate accumulation by shallow groundwaters occur from 5.3 to 3.8 Ma, a period over which $\delta^{18}O_{calcrete}$ values steadily increase by ~1‰. $\delta^{13}C_{calcrete}$ values from these same strata show significant swings with positive mean peak values of 0‰ (ca. 5 Ma) and 0.5‰ (ca. 4 Ma) separated by a trough with a mean value of −1.5‰ (4.5 Ma).

4. DISCUSSION

4.1. U-Pb Detrital Zircon Provenance in the West Kepintagh Section

The western Tarim Basin is bordered by the western Chinese Tian Shan to the north, Eastern Pamir to the west, and western Kunlun Shan to the south. We present data from 13 fluvial catchments that enter the Tarim Basin from (clockwise from south) the Hotan River (Kunlun Shan: Tb35, 1344), Yarkand River (Pamir: 1341, Tb38, Tb41, 1071-5, Tb43), Kirzlsu River (Pamir/Tian Shan nexus: Tb42), and Aksu River (Tian Shan: Tb45, Tb46, Tb48, Tb49, Tb50) (Carrapa et al., 2014; Blayney et al., 2016; Rittner et al., 2016; Fig. 7). Sample names are taken from each reference. Although we recognize that the topography today is different than during the Miocene and Pliocene, these active catchments may provide useful overviews of the zircon spectra for which to compare our samples. We do not show intermontane catchments from these reference studies because these are likely smaller and may have been more affected by drainage re-organization over time. Nor do we utilize eolian samples that may be influenced by variable wind patterns.

The three ranges (Kunlun Shan, Pamir, Tian Shan) all have complex U-Pb spectra (Fig. 7).

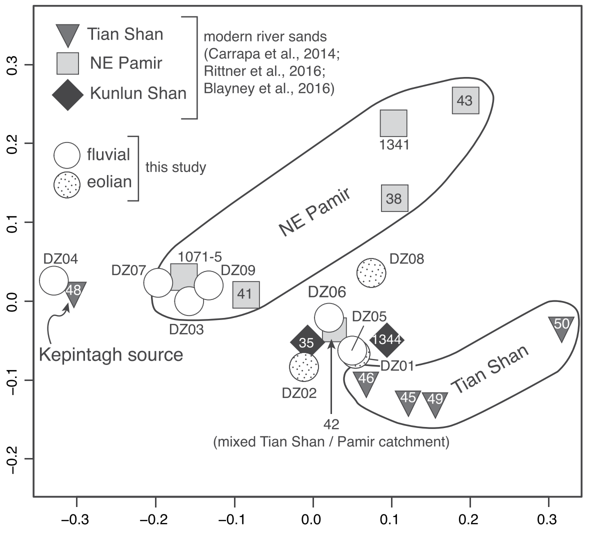

Figure 8. Multi-dimensional scaling map showing dimensionless Kolmogorov-Smirnov distances between detrital zircon (DZ) age distributions. The map is constructed such that the distances between pairs of points is positively correlated with the dissimilarity between sample age spectra. Samples from modern channels flowing into the western Tarim Basin (published sources) are compared with those from the western Kepintagh strata (this study). The polygons are drawn to indicate which groups of modern channels drain which mountainous sources (i.e., Tian Shan, Pamir). One sample, 48, is from a channel sand whose catchment is entirely in uplifted Paleozoic strata of the Kepitagh foreland.

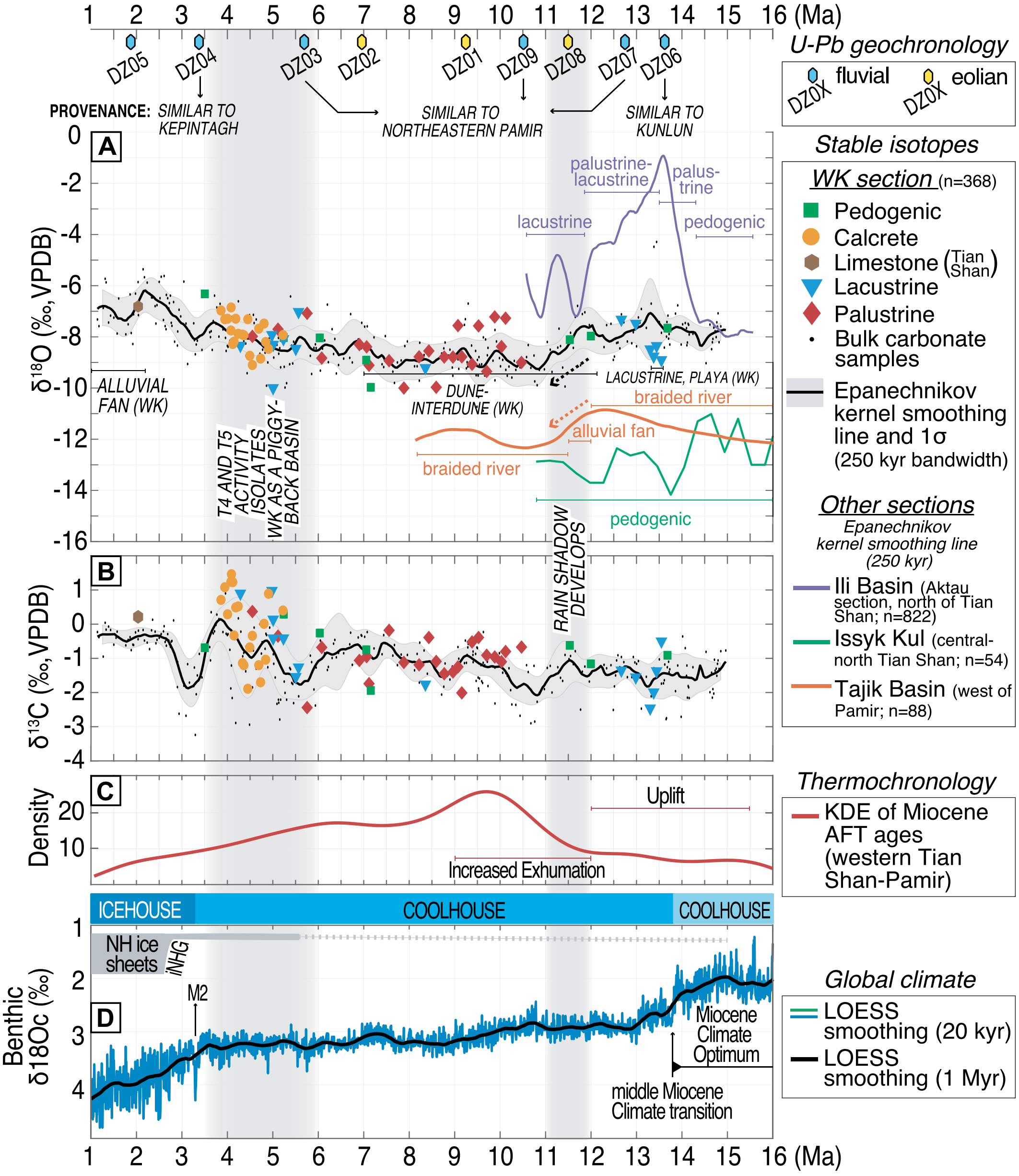

Figure 9. Mio-Pleistocene regional $\delta^{18}O_c$ and $\delta^{13}C_c$ values, thermochronology of the western Tian Shan-Pamir, and global climate change. (A and B) $\delta^{18}O_c$ and $\delta^{13}C_c$ values in this study (northwestern Tarim Basin) compared to compiled data from the Ili Basin (Aktau, north of Tian shan, Frisch et al., 2019), Issyk Kul (Tian Shan, Macaulay et al., 2016), and Tajik Basin (west of the Pamir-Tian Shan convergence zone, Li et al., 2022). (C) Kernel density estimate (KDE) plot of compiled regional apatite fission-track (AFT) ages (Jepson et al., 2021). (D) Compilation of benthic foraminifera $\delta^{18}O$ data as a proxy for global climate (Westerhold et al., 2020). Age model is from Heermance et al. (2018). Smoothed $\delta^{18}O_c$ and $\delta^{13}C_c$ lines include all samples and 68% confidence intervals are shown. WK—West Kepintagh; VPDB—Vienna PeeDee belemnite; NH—Northern Hemisphere; iNHG—intensification of Northern Heisphere Glaciation.

Kunlun samples are characterized by 150–250 Ma and 350–450 Ma peaks, with minor populations of 700–900 and 1800–2400 Ma. Eastern Pamir catchments contain populations of 200–300 Ma and 400–500 Ma with smaller peaks at 40 Ma and 110 Ma (Carrapa et al., 2014; Rittner et al., 2016; Blayney et al., 2016; Liu et al., 2017), as well as minor Precambrian peaks between 530 and 2500 Ma. Tian Shan samples are characterized by peak ages of 250–320 Ma, 400–500 Ma, and 700–900 Ma (Rittner et al., 2016), which is consistent with bedrock studies. Sample 48 stands apart from the other samples in its lack of a prominent 250–320 Ma peak and more diverse assemblage of Precambrian grains. This sample, however, is from a relatively small catchment confined to the Paleozoic and Cenozoic strata of the Kepintagh fold and thrust belt that surround this study. All the southern Tian Shan and its modern detritus lack Mesozoic and Cenozoic populations (Fig. 7). This is most likely due to the tectonic, especially plutonic, quiescence during the Triassic and Jurassic, and volcanic quiescence during the Cenozoic (Dumitru et al., 2001; Jolivet et al., 2010; Han et al., 2011).

The lack of unique U-Pb ages within the surrounding ranges makes provenance interpretation of our section challenging. The MDS plot provides a useful statistical comparison of these samples (Fig. 8). The Tian Shan and northeastern Pamir samples plot in separate zones. Samples DZ07, DZ09, and DZ03, which comprise the 13.0–6.0 Ma fluvial strata, all plot within the NE Pamir region (Fig. 8), and suggests that northeast flowing rivers (similar to the Yarkand River today, Fig. 7) provided the dominant source of fluvial sand to the study area. The Kunlun Shan samples plot between the Tian Shan and NE Pamir samples, as do all three eolian samples and DZ06 and DZ05. The oldest sample in our section (15.0 Ma) is probably derived from northward flowing rivers sourced from the Kunlun Shan in the middle-Miocene, similar to the Hotan River today. However, sample DZ05 within the Xiyu Conglomerate with a depositional age of 1.5 Ma is derived from alluvial fans that have prograded south from the Tian

Shan since the Miocene (Heermance et al., 2007; Charreau et al., 2009). Thus, although DZ grains may be recycled from older strata initially sourced from the Kunlun Shan or elsewhere, the current provenance of these grains must be from the Tian Shan margin. Moreover, DZ05 plots on the boundary of the Tian Shan zone in the MDS plot (Fig. 8), suggesting it could have a partial Tian Shan source. Therefore, the Xiyu conglomerate was sourced from either the adjacent basement of the Tian Shan or recycled from the uplifted Neogene foreland strata along the southern Tian Shan.

The only samples that do not plot as part of the Pamir or Tian Shan orogens in the MDS plot (Fig. 8) are samples DZ04 (3.5 Ma) and Tb48, the latter of which we have already described as having a catchment confined to the Paleozoic Kepintagh strata described in this study. However, the drainage area for Tb48 does not include any sediment from the Tarim Basin. Together, these results imply that by 3.5 Ma, the study area was isolated from the Tarim Basin and associated Pamir/Kunlun and high Tian Shan sediment sources. We infer this isolation to be due to uplift above the T4 structure that blocked any new input of sediment from more northerly Tian Shan sources, while simultaneous uplift above the T5 structure isolated the study area from the Tarim Basin. Our finding that the 3.5 Ma strata contains zircons from only the Kepintagh area suggests that uplift above the T4 and T5 structures occurred no earlier than 6.0 Ma, but before 3.5 Ma, bracketing deformation of the T4 and T5 structures. We therefore use 6.0 and 3.5 Ma as our max age #1 and max age #2, respectively, to calculate shortening rates across T4 and T5 (Table 1).

4.2. Neogene Depositional History and Paleoclimate Reconstruction

4.2.1. Carbonate Isotopic Composition as a Paleoclimate Record

The $\delta^{18}O_c$ and $\delta^{13}C_c$ compositions of interpreted lacustrine, palustrine, pedogenic, shallow groundwater carbonates (calcrete) and of bulk carbonate samples are shown in Figures 5 and 9 and presented in Table S1. Pedogenic carbonate $\delta^{18}O_c$ mainly reflects the isotopic composition of meteoric water, and $\delta^{13}C_c$ is mainly controlled by soil-respired CO_2 relating to paleovegetation cover (Cerling and Quade, 1993). Lacustrine carbonate $\delta^{18}O_c$ values reflect lake precipitation/evaporation ratios and $\delta^{18}O$ of inflow waters, whereas $\delta^{13}C_c$ reflects the isotopic composition of the dissolved inorganic carbon pool (Leng and Marshall, 2004). Palustrine carbonates originate from previous lacustrine/pond muds that are sub-aerially exposed and modified by pedogenic processes, and thus their $\delta^{13}C_c$ and $\delta^{18}O_c$ values tend to range between those of lacustrine/pond and pedogenic carbonates (Alonso-Zarza, 2003). $\delta^{18}O_c$ and $\delta^{13}C_c$ values of carbonate cement record surface conditions if cementation occurs under shallow burial conditions (Quade and Roe, 1999). The isotopic compositions of carbonate cements, both in pedogenically modified mudstones and in sandstones, have been used in several studies in the Tarim Basin as proxies for paleoclimate (e.g., Kent-Corson et al., 2009; Jolivet et al., 2018; Wang et al., 2020).

4.2.2. Modern Patterns of Precipitation on the Tian Shan and Northwestern Tarim Basin

The air regime over the Tian Shan region and northwestern Tarim Basin, in the broad region where our study section is located, is dominated by westerlies all year round rather than the Indian monsoon (Wang et al., 2017). The precipitation amount and stable isotopic composition of oxygen and hydrogen ($\delta^{18}O_p$, δD_p) on the Tian Shan and its northern and southern slopes are determined by rainfall seasonality and geographic position with respect to westerlies moisture transport (Wang et al., 2016a). The high elevation Tian Shan restricts the movement of westerlies into the arid leeward Tarim Basin, resulting in a much weaker transport of moisture via the lower atmosphere at the southern slope than at the northern slope (Wang et al., 2017). This produces different amounts of mean annual precipitation across the range. The central mountainous areas of the Tian Shan receive 409 mm, while the northern and southern basins receive only 277 mm and 66 mm, respectively (Shi et al., 2008). All regions receive most of this rainfall during the warmest half of the year (April to October), whereas precipitation is very low during the winter (Wang et al., 2016a, 2016b). An observation network of 23 stations established around the Tian Shan from 2012 to 2013 (Wang et al., 2016a) and data from Global Network of Isotopes in Precipitation (IAEA/WMO, 2020) provides an overview of the seasonal and spatial changes in $\delta^{18}O_p$ and δD_p around the Tian Shan. Both annual and long-term regional observations of isotopes in precipitation indicate that summer $\delta^{18}O_p$ values are higher than those during winter on both northern and southern sides of the Tian Shan (Tian et al., 2007; Wang et al., 2017). The $\delta^{18}O_p$ of stations near our study area are shown in Figure 1. Modern summer $\delta^{18}O_p$ values are highest and d-excess values are lower on the arid southern slopes, where sub-cloud evaporation processes dominate (Wang et al., 2016b; Bershaw, 2018). Meanwhile, on the northern and mountainous windward regions, $\delta^{18}O_p$ values decrease and d-excess increases with elevation (Bershaw, 2018). During winter, precipitation becomes isotopically depleted in the arid regions to the south of the Tian Shan due to development of an isotopic rain shadow (Wang et al., 2016a, 2016b). These observations provide a baseline for comparison of Miocene and Pliocene isotope records from the northern and southern Tian Shan.

4.2.3. Depositional History and Isotope-Based Paleoclimate Reconstruction

The combination of sedimentology, sediment provenance and carbonate stable isotope geochemistry in this study document the depositional and paleoclimate history of the western Tarim Basin since the early Miocene (Fig. 10). At the base of the WK section, thick lacustrine strata (Unit C and lower Pakabulake Formation) indicate wet environments prevailed prior to the development of the Taklimakan Desert. A transition to more arid conditions with shallowing of the lacustrine system unfolded just before the erg-system formed, as indicated by an increase in lacustrine $\delta^{18}O_c$ from ca. 13.5 Ma ($-8.6 \pm 0.3‰$) to ca. 12.5 Ma ($-7.4 \pm 0.1‰$) and coarsening of sediments. Subsequently, the erg-system developed and lacustrine $\delta^{18}O_c$ values decreased from 8.6 to 8.2 Ma based on values measured in carbonates from an interdune lake ($-9.2 \pm 0.1‰$) and shallow ponds ($-9.1 \pm 0.8‰$). Since an increase in $\delta^{18}O_c$ values would be expected in more arid environments with increased evaporation/precipitation ratios (Leng and Marshall, 2004), this decrease in lacustrine $\delta^{18}O_c$ values is interpreted to indicate that lake water must have been derived from high, mountainous areas depleted in ^{18}O. Lacustrine $\delta^{18}O_c$ and $\delta^{13}C_c$ values increase after 5.5 Ma and become very similar to values in calcretes, interpreted to have precipitated from shallow groundwater. $\delta^{13}C$ values during this time show a significant increase of up to 2.5‰ to mean values around 0‰.

In pedogenic carbonates, $\delta^{18}O_c$ values of ~–8‰ in the early stages of desert formation (pre-11.5 Ma) decrease by up to 1.5‰ by the time the desert was expanding southward (ca. 7 Ma) and aridification increased in the Tarim Basin (e.g., Sun et al., 2017). Since pedogenic $\delta^{18}O_c$ is a proxy for the isotopic composition of soil-penetrating meteoric water (Cerling and Quade, 1993), relatively higher pedogenic $\delta^{18}O_c$ would be expected in arid settings (e.g., dune deserts) compared to wetter settings due to increased evaporation. Thus, a decrease of 1‰–2‰ in interdune pedogenic $\delta^{18}O_c$ values from ca. 12 to 7 Ma suggests evaporation-related ^{18}O enrichment of soil-penetrating water may have been concealed by a decrease in the $\delta^{18}O$ values of meteoric water. The highest pedogenic $\delta^{18}O_c$ value of $-6.3‰$ occurs at ca. 3.5 Ma, inter-

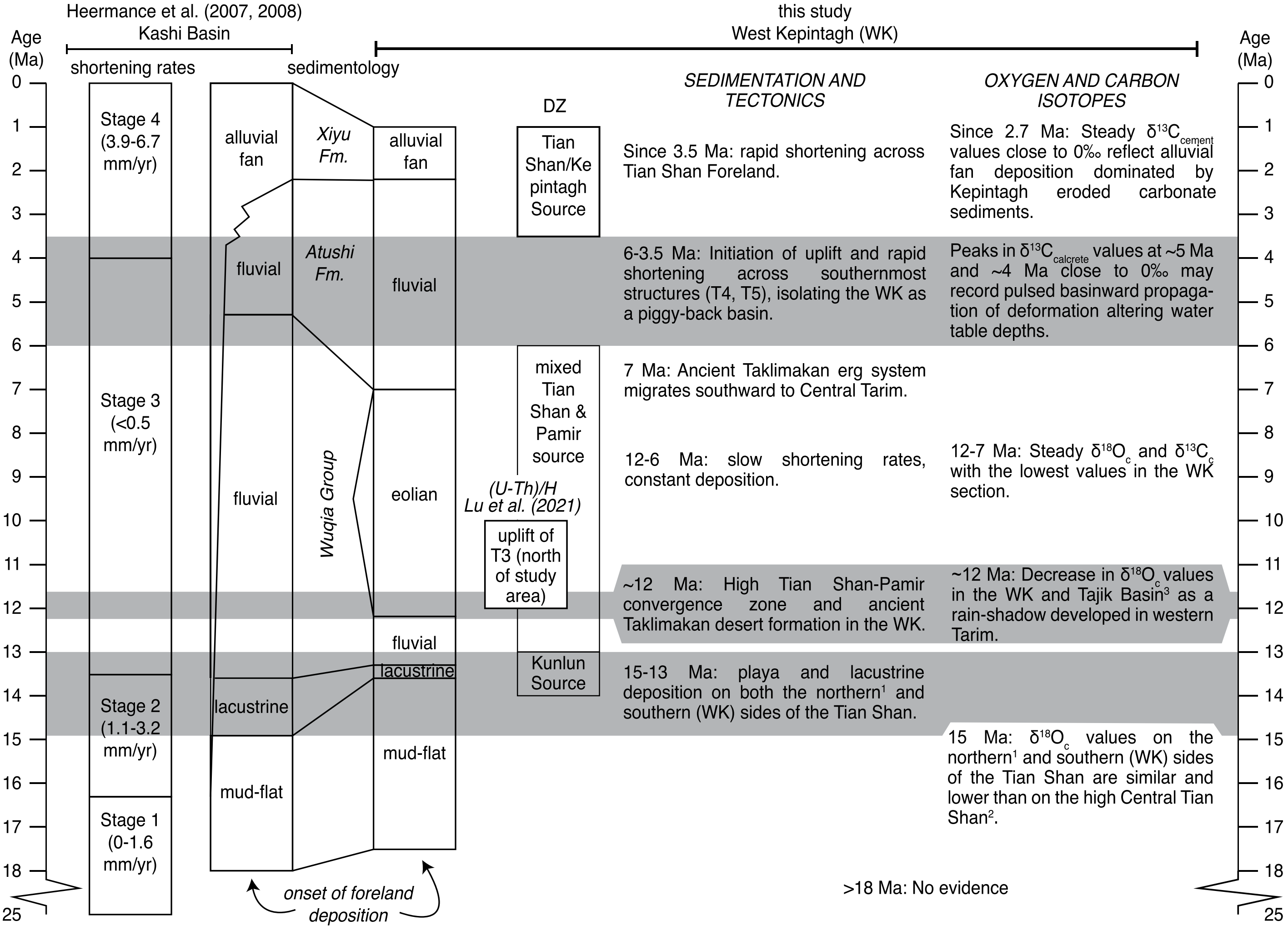

Figure 10. Summary of shortening rates, sedimentology, tectonics, and stable isotopic composition of carbonates in the western Tarim Basin. Fm.—Formation.

preted to reflect intensified aridification similar to modern conditions. Before ca. 11.5 Ma, bulk carbonate mudstone samples have $\delta^{18}O_c$ values that are similar to pedogenic values and higher than values in lacustrine carbonates (at ca. 13.5 Ma). Fluvial and eolian samples from 15, 12.7, and 11.5 Ma show poor cementation, high intergranular volume and low percentage of carbonate grains (<6%–12%) in point counts from thin-sections (Vilkas, 2019). This suggests that $\delta^{18}O_c$ values in bulk carbonate samples mainly reflect the $\delta^{18}O$ of surface waters or very early cementation under shallow burial conditions, similar to pedogenic carbonates, and thus they are used as paleoclimate proxies in this study (Cerling and Quade, 1993; Quade and Roe, 1999).

From 12.2 to 7.0 Ma, dune and damp interdune deposits predominate. These conditions result from progressive rise in the relative water table during ongoing dune and interdune migration (Mountney, 2012). Palustrine carbonates from damp/wet interdune settings in this study are interpreted to have formed after rises in the water table allowed accumulation of floodplain and overbank muds subjected to intermittent desiccation and pedogenic modification. Mudstone lithofacies interpreted as overbank deposits are interbedded with fluvial sandstones that locally show ripples (for instance, at 8.2, 6.9, 5.1, and at 9.7 Ma) (Fig. 3). During the process of palustrine carbonate formation from surface waters and surficial groundwaters, the original $\delta^{18}O$ of carbonates formed in subaqueous settings is modified by soil processes and/or early meteoric diagenesis (either phreatic or vadose) (Alonso-Zarza, 2003). In the dune-interdune system from 12.2 to 7.0 Ma, the highest pedogenic $\delta^{18}O_c$ values occur at ca. 12 Ma and the lowest at ca. 7 Ma, with most of the palustrine $\delta^{18}O_c$ having values between these pedogenic values. Interdune palustrine mudstones ($\delta^{18}O_c = -8.6 \pm 0.8‰$) are interbedded with carbonate-cemented eolian sandstones (eolian bulk carbonate samples: $\delta^{18}O_c = -8.9 \pm 0.7‰$). A previous study showed that eolian sandstone samples show low intergranular volume (at 10.5 and 9.5 Ma) and low extrabasinal (detrital) carbonate content (5% at 9.5 Ma) (Vilkas, 2019). Thus, palustrine and bulk carbonate $\delta^{18}O_c$ values likely reflect the $\delta^{18}O_c$ of surface (meteoric) waters and surficial groundwaters (Alonso-Zarza, 2003) feeding interdune settings. Vilkas (2019) showed that a few sandstone samples have relatively high extrabasinal carbonate content (20%–26%) at ca. 10.5, 7, and 6 Ma, and heavy cementation at 7 and 6 Ma (Vilkas, 2019). These may indicate some local detrital contamination and cementation under deeper burial conditions in sandstones, particularly those of the lower Atushi Formation. Further studies with a more detailed sedimentary petrography are needed to understand the extent and character of detrital input and cementation both in sandstones and mudstones of the WK.

From 5.6 to 3.9 Ma, lacustrine, calcrete, and cement carbonates predominate. The siltstone and sandstone rocks hosting the discontinuous calcrete lenses at ca. 3.4 Ma are heavily cemented by carbonate and contain 6% extrabasinal carbonate (Vilkas, 2019). Calcrete and cement (bulk carbonate samples) are interpreted to have precipitated in the capillary fringe zone near the water table surface and their $\delta^{13}C_c$ likely reflects bicarbonate-rich groundwater (Wright and Tucker, 1991). Post 2.7 Ma samples from interbedded sandstone lenses within the Xiyu Formation strata have $\delta^{13}C_c$ values that match those of carbonate clasts derived from the Tian Shan ($\delta^{13}C = 0.2‰$), and likely reflect detrital or dissolved-reprecipitated carbonate from Paleozoic carbonate (e.g., Thompson et al., 2015; Heermance et al., 2007).

4.3. Pulsed Deformation and Shortening Rates

Our results allow us to place new constraints on shortening rates within the Tian Shan foreland at the longitude of the WK section (Table 1). Total shortening across all foreland structures is 35.3 ± 3.5 km. This shortening estimate is identical to that of Allen et al. (1999) and within the minimum (~23 km) and maximum (~50 km) values presented in Yin et al. (1998) and McKnight (1993). Deformation above fault T3 initiated at ca. 12 Ma based on thermochronology (Lü et al., 2021), and not until after 6.0 Ma for T4 and T5. Therefore, average shortening rates since 12 Ma are ~3 mm/yr. However, T4 and T5 did not initiate until between 6.0 and 3.5 Ma, and T5 is likely still active today, so shortening rates across the T4 and T5 structures are between 3.9 and 6.7 mm/yr, much faster than the long-term shortening rates (Table 1). This result suggests that shortening rates have increased since the Pliocene in the Tian Shan foreland.

4.4. Tectonic and Paleoclimate History of the Kepintagh Foreland

4.4.1. Early to Middle Miocene (25–13.6 Ma)

Neogene sedimentation in the Tian Shan foreland at the study location began at ca. 15.1 Ma with deposition of fluvial sediments sourced from the southwest, likely the Kunlun Shan and/or Pamir. Although DZ06 from 15 Ma does not preclude a mixed Tian Shan/Pamir source, the sample is similar to the Kunlun Shan samples and paleocurrent data indicate a source from the southwest, suggesting a northeast flowing, trans-Tarim Basin fluvial system originating in the Kunlun Shan similar to the Hotan River today (Fig. 7). $\delta^{18}O_c$ values from carbonate cement (−7.8 ± 0.4‰) between 15.1 and 13.6 Ma in the WK section are similar to pedogenic carbonates (~−8‰) in the Aktau section north of the Tian Shan (Ili Basin, Frisch et al., 2019) and suggest that the northern and southern Tian Shan were receiving rainfall with similar $\delta^{18}O$ at ca. 15 Ma (Figs. 9A and 11D). Meanwhile, in the central Tian Shan, relatively depleted pedogenic $\delta^{18}O_c$ values in Issyk Kul (~−11 to −13‰; Macaulay et al., 2016) suggest rainfall at that location had much more negative $\delta^{18}O$ values (Figs. 9A and 11D). Indeed, depleted values in Issyk Kul have been interpreted to reflect orographically enhanced precipitation due to surface uplift accompanying deformation and rock uplift in the Terskey Range (Macaulay et al., 2016). Such a precipitation pattern in northern, southern, and central Tian Shan differs from the modern pattern, which shows increasing $\delta^{18}O$ values from north to south over the mountain belt (Fig. 1). This pattern indicates that, by ca. 15 Ma, moisture bearing winds were branching around the already high-elevation central Tian Shan (Fig. 11D), and the low-level westerly winds were able to penetrate the Tarim Basin. The south Tian Shan fault, confined to basement north of the Kepintagh fold-and-thrust belt and our study area, may have been active from 24 to 15 Ma (Jia et al., 2015; Sobel et al., 2006), indicating that some topography had developed in the Central Tian Shan to the north, consistent with Issyk Kul pedogenic carbonates recording depleted $\delta^{18}O_c$ values typical of relatively more elevated regions. Coevally in the northwestern Pamir, deformation initiated on the Main Pamir Thrust (MPT) ca. 25–18 Ma, with formation of several imbricate faults ahead of the MPT during the Miocene (Thompson Jobe et al., 2018). However, in the region between the northeastern Pamir and the southwestern Tian Shan, deformation was still incipient and the Pamir-Tian Shan convergence zone showed low relief, limited topography, and restricted alluvial fan deposition (Chen et al., 2019; Heermance et al., 2018; Wang et al., 2014) (Figs. 11C and 11D).

Together, these data suggest that during the early-middle Miocene (ca. 25–13.6 Ma), the Tarim Basin was likely much wider (N-S) and connected to the Fergana, Gulcha, and Alai basins to the west (Bande et al., 2017). The Kunlun/Pamir ranges to the south and west likely contributing the bulk of sediment into the basin. A relatively narrow but high Tian Shan was located at approximately the latitude of Lake Issyk Kul. Uplift (and sedimentation) along the southern Tian Shan initiated at ca. 18 Ma to the west of this study near Kashgar (Heermance et al., 2008), although deformation had not yet occurred within the foreland at the longitude of this study. The westerlies provided isotopically similar precipitation to both the northern and southern Tian Shan, with depleted $\delta^{18}O_c$ at higher elevations. Deformation of the Tian Shan must have been confined to much narrower and more northerly regions than today. Miocene alluvial fan deposits derived from the Tian Shan are first observed within the Tarim Basin at 15.5 Ma, ~50 km north of Kashgar, suggesting that the Tian Shan Mountain front was located well north of the Pamir and the study area at this time (Figs. 1 and 11D; Heermance et al., 2007).

4.4.2. Middle to Late Miocene (ca. 13.6–7.0 Ma)

Sedimentation changed abruptly in the study area at 13.6 Ma to gypsiferous lacustrine deposits. Lacustrine strata were deposited from 13.6 to 13.3 Ma, are at least 50 m thick, and are continuous for at least 150 km to the west where they are observed in the Kashgar basin (Reservoir section of Heermance et al., 2007). This suggests a regional shift in depositional environment from fluvial to lacustrine. Coeval and similar strata are found ~600 km northeast on the northern flank of the Tian Shan from ca. 13.6 to 13.3 Ma (Ili Basin and northwestern Tarim; Fig. 11D; Frisch et al., 2019). At 13.3 Ma in both the Kashgar and western Kepintagh regions, depositional environments changed to a generally east-west trending meandering fluvial system that likely represented range-parallel flow along an underfilled flexural basin related to thrust-faulting along the southern margin of the Tian Shan north of the study area (Heermance et al., 2008; Lü et al., 2021). Sand dune strata appear in the study section at 12.2 Ma and pinch-out laterally toward the west into the fluvial strata (Heermance et al., 2018). In contrast, at ca. 12.6 Ma in the Ili basin a perennial lake formed, implying that, after 13 Ma, the northern Tian Shan became wetter whereas the southern Tian Shan became drier. Meanwhile, on the western side of the Pamir, in the Tajik Basin, abrupt sediment coarsening and detrital source change took place at 13.5 Ma and 12 Ma, respectively (Li et al., 2022). Strikingly, all three changes in depositional environments (Western Tarim, Ili Basin, and Tajik Basin) were characterized by an overall decrease in $\delta^{18}O_c$ values. Decreasing values on the northward Ili Basin are consistent with its local positive water budgets, interpreted by Frisch et al. (2019) to represent enhanced supply of moisture windward by stronger westerlies during and after the middle Miocene Climate Transition (mMCT) (Figs. 9A and 9D). However, a post–12 Ma decreasing trend in $\delta^{18}O_c$ on the southward Tarim Basin coincident with desertification contrasts with the coeval increasing trend in $\delta^{18}O_c$ values of +2.5‰ in the Qaidam Basin and in the Northern Tibetan Plateau, linked to intensified aridification (e.g., Zhuang et al., 2011). Increasing values in the WK would also be expected during desertification due to enhanced evaporative effects, much

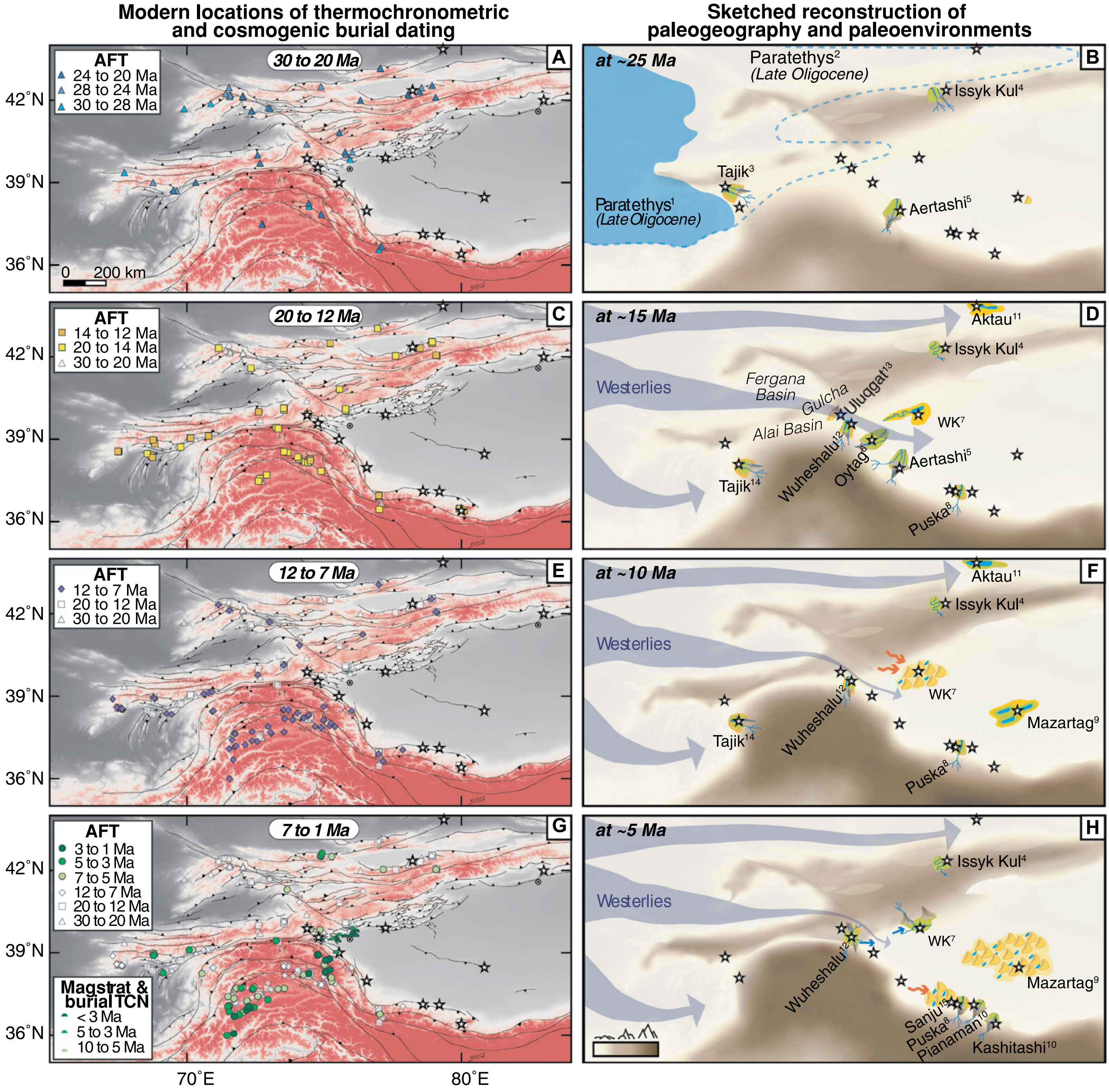

Figure 11. Late Cenozoic tectonic and paleoenvironmental evolution of the Pamir, Tian Shan, and Tarim Basin since the Oligocene. Panels A, C, E, and G show times and locations of inferred deformation and exhumation based on compiled apatite fission track (AFT) data (references in Supplemental Data 1; see text footnote 1) and combined magnetostratigraphy and cosmogenic burial dating (terrestrial cosmogenic nuclides, TCN) data (Thompson Jobe et al., 2018). Panels B, D, F, and H show a regional paleogeographic and paleoenvironmental reconstruction at ca. 25, 15, 10, and 5 Ma, respectively (descriptions in Table S2; see footnote 1). Stars denote study sites in previous studies, as follows. 1—Popov et al. (2010); 2—Li et al. (2020); 3—Wang et al. (2019); 4—Macaulay et al. (2016); Cobbold et al. (1994); 5—Blayney et al. (2016); 6—Bershaw et al. (2012); 7—Heermance et al. (2018); 8—Kent-Corson et al. (2009); 9—Sun et al. (2009, 2017); 10—Graham et al. (2005); 11—Ili Basin, Frisch et al. (2019); 12—Chen et al. (2019); 13—Wang et al. (2014); 14—Li et al. (2022); 15—Sun and Liu (2006).

like modern summer precipitation signals that are dominated by sub-cloud evaporation processes (Fig. 1; Wang et al., 2016a; Bershaw, 2018).

Several lines of evidence indicate that the western Tian Shan and northeastern Pamir region experienced widespread deformation from ca. 16 to 12 Ma. Just west of our study area in the Kashgar basin thrust, southward propagation of the deformation front and initiation of the

Kashgar Basin thrust occurred at 16.3 ± 0.5 Ma (Heermance et al., 2008), with rapid exhumation and shortening near the westward continuation of this thrust based on apatite fission track cooling ages (13.6 ± 2.2 Ma; Sobel and Dumitru, 1997) and an increase in sediment-accumulation rate of middle Miocene sediments (ca. 12 Ma; Chen et al., 2015). (U–Th)/He thermochronology ~200 km north of the study area in the Terskey, Sarajaz, and Kyrgyz ranges within the high Tian Shan suggest increased exhumation and cooling at ca. 15–5 Ma (Bullen et al., 2001; Macaulay et al., 2014). 30 km north of this study, (U–Th)/He thermochronology data from fault T3 suggests initiation of the Tian Shan foreland did not occur until 12 Ma (Figs. 1 and 4; Lü et al., 2021). Moreover, any earlier uplift or deformation at this longitude did not involve any known Neogene sedimentation into the Tarim Basin and was likely limited to the high Tian Shan basement which translated south after ca. 12 Ma. In the Tajik basin, detrital zircon U- Pb age spectra, mudstone bulk-rock εNd values and $\delta^{18}O_c$ and $\delta^{13}C_c$ data suggest that the North Pamir experienced a middle-late Miocene phase of deformation and surface uplift (Li et al., 2022). Low temperature thermochronology age data compiled in this study (kernel density estimate plots in Fig. 9C; Jepson et al., 2021) also support substantial uplift linked to deformation on the mountain ranges surrounding the western Tarim Basin from 16 to 12 Ma. This mid- to late Miocene widespread period of deformation was followed by a substantial increase in exhumation after 12 Ma (Fig. 9C), partitioning of the convergence zone into discrete basins from 12 to 8 Ma (Figs. 11C–11F), and increase in sediment accumulation rates in the Tian Shan foreland (e.g., Bande et al., 2017; Heermance et al., 2007).

During the second phase of widespread deformation in the mid- to late Miocene (e.g., Bande et al., 2017; Heermance et al., 2008; Thompson Jobe et al., 2018; Jepson et al., 2018), Earth's climate was experiencing the mMCT from the warm Miocene Climate Optimum (17–14 Ma) toward a more pronounced coolhouse state (Fig. 9D; Westerhold et al., 2020). Isotopic values in this study, however, do not show any significant shift at the time of more pronounced cooling (ca. 14 Ma). Rather values seem to respond to younger (ca. 12 Ma onward) tectonic and local environmental deposition changes. Therefore, between 15 and 12 Ma in our study area, the observed tectonic, environmental, and isotopic changes appear decoupled from global climate changes (Fig. 9).

Decreasing mean $\delta^{18}O_c$ values in the WK at ca. 12 Ma coeval to desertification may be explained by three factors. First, the onset of an isotopic rain shadow (Blisniuk and Stern, 2005) on the leeward side of the Pamir-Tian Shan (Bougeois et al., 2018; Heermance et al., 2018) due to surface uplift of the convergence zone and restriction of westerly windflow into the Tarim Basin (Fig. 11F). Moist air masses forced to ascend over orography would undergo Rayleigh distillation, decreasing $\delta^{18}O$ values in precipitation as they rise in elevation (Rowley and Garzione, 2007). Strong westerly winds needed for erg development would still cross over the Tian Shan and channel through the convergence zone, as suggested by wind paleodirections in the WK (Heermance et al., 2018; Fig. 5), our detrital zircon U-Pb data (Figs. 6 and 8) and gradual increase in the grain size of eolian particles in Uluqgat (Fig. 11F; Wang et al., 2014). Orographic precipitation, however, would have modified these winds into drier and more ^{18}O-depleted air masses (Blisniuk and Stern, 2005). In the Tajik Basin, a recent study has also attributed a negative excursion in $\delta^{18}O_c$ between 12 and 10 Ma to enhanced orographic precipitation, decreased sub-cloud evaporation (Li and Garzione, 2017) and lower precipitation temperature (Bershaw and Lechler, 2019), which they attribute to surface uplift of the north Pamir (Li et al., 2022). Second, Pamir-Tian Shan deformation and exhumation may have increased basinward run-off of highly ^{18}O-depleted waters that most often occur at high-elevations. Such changes in the distribution of precipitation of basin drainages have been invoked to explain isotope shifts in other Central Asian basins (e.g., Jolivet et al., 2018; Charreau et al., 2012). Finally, basin inflow of ^{18}O-depleted waters may have masked the signals of evaporative processes at the early stages of desert formation when the erg system appears to have been restricted to the northwestern Tarim Basin (Fig. 11F). Together, these data support the development of a rain shadow eastward of an amalgamated Tian Shan/Pamir Mountain range after 12.2 Ma.

From 12 to 7 Ma, $\delta^{18}O_c$ values in dune-interdune deposits in the WK section are the lowest observed (mean = -8.7 ± 0.7‰) and have the smallest variability in our record. These low isotopic values contrast with positive isotopic excursions in other basins to the east (Qaidam Basin and Northern Tibetan Plateau) as they were becoming increasingly arid (e.g., Zhuang et al., 2011). U-Pb detrital zircon data suggests that from 13 to 6 Ma, fluvial sediment was sourced predominantly from the northeastern Pamir (MDS in Fig. 8), i.e., the Pamir-Tian Shan convergence zone, much like the modern Kirzlesu and Yarkand rivers that drain into the western Tarim Basin today. The shift to more negative $\delta^{18}O_c$ values at 12 Ma followed by steady low isotopic values after 7 Ma, in addition to the shift in provenance to the Pamir-Tian Shan convergence zone, argues for the hypothesis that a rain-shadow developed in the WK as the convergence zone became higher in elevation. Li et al. (2022) similarly interpreted a coeval negative carbonate $\delta^{18}O$ excursion and sediment provenance change in the Tajik Basin (Fig. 9) to record uplift of northeastern Pamir and enhancement of the process of Rayleigh distillation.

4.4.3. Late Miocene to Present (7.0–0 Ma)

Abruptly at 7 Ma, eolian dune strata disappear from the WK section and are replaced with channelized fluvial and floodplain deposition, although the sediment source remains unchanged for fluvial samples (Fig. 8, DZ03, DZ07, DZ09) between 13 and 6 Ma. An abrupt change in the detrital zircon spectra occurs between 6 and 3.5 Ma, where provenance switches from a mixed Tian Shan-Pamir source to a local, Kepintagh source. By this time, not only was the study area shut off from the Kunlun and/or Pamir sediments that fill the Tarim Basin, but must have also been disconnected from more northerly catchments within the southern Tian Shan that characterize samples Tb45, Tb46, Tb49, and Tb50 (Rittner et al., 2016). These changes are consistent with the initiation of uplift and deformation above the two frontal foreland faults T4 and T5 between 6 and 3.5 Ma (Fig. 4) interpreted to have isolated the WK as a piggy-back basin that received sediments from the Kepintagh basement only (Fig. 9).

Deformation in our study area parallels widespread deformation in the Tian Shan foreland after ca. 7 Ma. West from the WK, sedimentation rates markedly increased at ca. 7 Ma in the Kashgar depression and in the northeastern Pamir-Tian Shan converge zone (Qiao et al., 2016, 2017); deformation initiated in the Kelatuo (>5 Ma), Keketamu (3.9–4.0 Ma), Atushi (ca. 3.8 Ma), and Kashgar (ca. 1.4 Ma) anticlines (Heermance et al., 2008; Thompson Jobe et al., 2018); and the Pamir Frontal Thrust initiated from 6 to 5 Ma (Thompson et al., 2015; Thompson Jobe et al., 2018). East of the WK, deformation in the Kuqa fold-and-thrust belt jumped southward at 5.5 Ma and shortening rates increased 200%–300% (Hubert-Ferrari et al., 2007; Li et al., 2012; Zhang et al., 2014). Plio-Pleistocene deformation is marked by rapid progradation of the time-transgressive Xiyu conglomerate into the Tarim Basin, including at this study location at 2.2 Ma (Heermance et al., 2008; Thompson Jobe et al., 2018). We interpret deformation above the two southernmost imbricate structures to have initiated after 6.0 Ma, suggesting a rapid southern shift of deformation and increase in shortening rates since that time. In the study area, deformation lasted at least until ca. 1.0 Ma, based on the observation of growth strata (Fig. 3).

Plio-Pleistocene carbon isotope excursions in carbonates are interpreted to reflect deformation in the WK area. Positive peaks in $\delta^{13}C_c$ values in calcrete (shallow groundwater) and shallow lacustrine carbonates in WK occur at ca. 5 Ma (−1 ± 1.1‰) and ca. 4 Ma (−0.2 ± 0.9‰), and in sandstone carbonate cement after ca. 2.7 Ma (−0.4 ± 0.3‰) (Fig. 9B). Values are similar to the $\delta^{13}C_c$ value of 0.2 ± 0.1‰ in Tian Shan limestone clasts analyzed in this study (Figs. 9B). We speculate that Tian Shan foreland deformation exhumed Paleozoic strata in the thrust sheets of the Kepintagh fold-and-thrust belt, increased the mountain-to-basin hydraulic gradient and raised the water table in the proximal foreland to a point where calcretes precipitated in evaporative capillary fringe zones near the surface (Wright and Tucker, 1991). Calcrete $\delta^{13}C_c$ values close to 0‰ at ca. 5 Ma and ca. 4 Ma may reflect heavy cementation by groundwater enriched in dissolved bicarbonate derived from emergent Paleozoic carbonate. Finally, after 2.7 Ma, remarkably constant $\delta^{13}C_c$ values ranging from −1 to 0‰ in sandstone carbonate cement of the upper Atushi and Xiyu formations (Figs. 5 and 9B) are interpreted to derive from detrital or reprecipitated Kepintagh/Tian Shan limestone clasts, often encountered in Xiyu strata (e.g., Heermance et al., 2007). Detrital zircon spectra for the uppermost samples (DZ05) record recycled grains from the Neogene foreland sediments.

5. CONCLUSIONS

New stratigraphic, structural, U-Pb detrital zircon, and stable oxygen and carbon isotope data from a continuous 3800-m-thick section of the Tian Shan foreland document the complex interaction between regional climate and tectonic changes since the early Miocene (summarized in Fig. 10). Depositional environments and basin water isotopic composition were controlled by the far-field influences of westerly atmospheric currents and Pamir tectonics from 15.1 to 13.6 Ma. Basins northward (Ili Basin, Frisch et al., 2019) and southward (WK) of the Tian Shan were likely receiving rainfall of similar compositions at ca. 15 Ma and had similar playa-lacustrine environments from ca. 13.6 to 13.3 Ma (Fig. 11D). Our oldest detrital zircon samples suggest sediments were derived from Kunlun-sourced northward flowing rivers analogous to the modern Hotan River (Fig. 7) by ca. 13.6 Ma, instead of the eastward flowing rivers that drain into the modern western Tarim Basin. Combined with structural, low temperature thermochronology and sedimentological data from previous studies (Bande et al., 2017; Chen et al., 2019; Heermance et al., 2018; Wang et al., 2014; Jepson et al., 2021), these data suggest that westerly atmospheric flow was not or was only partially blocked by the then low-elevation Pamir-Tian Shan convergence zone at that time. Subsequently, fluvial sediment source changed to the northeastern Pamir in the Pamir-Tian Shan convergence zone, after which paleoenvironmental conditions on the Tian Shan flanks began to diverge into wetter (Ili Basin to the north, Frisch et al., 2019) and drier (WK to the south, this study) conditions at ca. 12.6 and 12.2 Ma, respectively. WK sand dune desert formation at 12.2 Ma is coincident with uplift and deformation of the foreland just north of the study area, and indicates a temporal relation between uplift and aridification of the foreland. The southern Tian Shan margin may have created a backstop that trapped sand derived from the west. Furthermore, the paucity of Neogene strata east of the Piqiang fault suggests that the eastern half of the Kepintagh thrust belt may have been at higher elevation and sand dunes collected in the re-entrant between the southern Tian Shan and eastern Keptintage, similar to the environment in the Great Sand Dunes of Colorado (USA). The negative $\delta^{18}O_c$ isotopic excursion after ca. 12 Ma on the western Tarim Basin presented in this study is coeval with a negative $\delta^{18}O_c$ isotopic excursion in the Tajik Basin, just west of the Pamir, which experienced a sediment source change from the Central to North Pamir at that time (Li et al., 2022). In the WK, between 12 and 7 Ma, $\delta^{18}O_c$ values in dune and interdune WK deposits remained the lowest throughout our record. Such negative $\delta^{18}O_c$ trends accompanying desertification of the western Tarim Basin contrast with late Miocene increasing trends in $\delta^{18}O_c$ values of +2.5‰ in the Qaidam Basin and Northern Tibetan Plateau, also linked to intensified aridification (e.g., Zhuang et al., 2011). These suggest that the Pamir-Tian Shan orogen began to obstruct low-level westerly windflow into the Tarim Basin by ca. 12 Ma, indicating the formation of an isotopic rain shadow east of the Pamir-Tian Shan convergence zone and increased run-off of ^{18}O-depleted waters from exhuming high-elevation regions, which masked the signals of evaporative processes on the still incipient Taklimakan desert from 12 to 7 Ma (Figs. 9A, 11D, and 11F). After 7 Ma, rapid uplift and widening of the Tian Shan caused a shift in paleoenvironments to fluvial and floodplain systems as the erg system was pushed southward to central and southwestern Tarim (Fig. 11H). From ca. 6 to 3.5 Ma, the dominant sediment provenance shifted from the northeastern Pamir to purely Kepintagh source by 3.4 Ma (Figs. 8 and 9), as shortening rates increased in the foreland to 3.9–6.7 mm/yr. Over that time, positive $\delta^{13}C_c$ excursions to values close to ∼0‰ took place in fluvial, floodplain, and alluvial fan deposits in the WK section. These excursions are interpreted to reflect changes in hydrology and sediment provenance that are linked to deformation across faults T4 and T5 (6–3.5 Ma) in the Tian Shan foreland that isolated the WK as a piggy-back basin, as shortening rates increased ∼3-fold across the region (Figs. 4, 11G, and 11H) (e.g., Thompson Jobe et al., 2018; Heermance et al., 2008). We have shown that these changes in carbonate stable isotope composition, paleoenvironments, and sediment provenance in the WK appear to be decoupled from pronounced late Cenozoic global climate changes (Fig. 9D), but are linked to uplift of the surrounding mountain ranges. This work highlights the relative influence of local versus regional signals within a foreland basin and suggests that local tectonics may dominate over the more regional and global climate signals in active tectonic settings.

ACKNOWLEDGMENTS

This project was supported by an American Chemical Society Petroleum Research Fund Grant to Heermance (#50776-UN18), and National Science Foundation grants to Heermance (#1348075), Garzione (#1348005), and Cecil (#1655152). Alex Pullen is thanked for his assistance with isotopic analysis at the University of Rochester, New York, USA. We thank the Science Editor Dr. Mihai Ducea, the associate editor Galen Halverson, reviewer Dr. Edward Sobel, and another anonymous reviewer for their insightful comments and suggestions that helped improve the manuscript significantly.

REFERENCES CITED

Allen, M.B., Vincent, S.J., and Wheeler, P.J., 1999, Late Cenozoic tectonics of the Kepingtage thrust zone: Interactions of the Tien Shan and Tarim Basin, northwest China: Tectonics, v. 18, p. 639–654, https://doi.org/10.1029/1999TC900019.

Allmendinger, R.W., 1998, Propagation folds footwall synclines: Tectonics, v. 17, p. 640–656, https://doi.org/10.1029/98TC01907.

Alonso-Zarza, A.M., 2003, Palaeoenvironmental significance of palustrine carbonates and calcretes in the geological record: Earth-Science Reviews, v. 60, p. 261–298 https://doi.org/10.1016/S0012-8252(02)00106-X.

Amidon, W.H., and Hynek, S.A., 2010, Exhumational history of the north central Pamir: Tectonics, v. 29, p. 1–13, https://doi.org/10.1029/2009TC002589.

Bande, A., Sobel, E.R., Mikolaichuk, A., Schmidt, A., and Stockli, D.F., 2017, Exhumation history of the western Kyrgyz Tien Shan: Implications for intramontane basin formation: Tectonics, v. 36, p. 163–180, https://doi.org/10.1002/2016TC004284.

Bershaw, J., 2018, Controls on deuterium excess across Asia: Geosciences (Switzerland), v. 8, https://doi.org/10.3390/geosciences8070257.

Bershaw, J., and Lechler, A.R., 2019, The isotopic composition of meteoric water along altitudinal transects in the Tian Shan of Central Asia: Chemical Geology, v. 516, p. 68–78, https://doi.org/10.1016/j.chemgeo.2019.03.032.

Bershaw, J., Garzione, C.N., Schoenbohm, L., Gehrels, G., and Tao, L., 2012, Cenozoic evolution of the Pamir plateau based on stratigraphy, zircon provenance, and stable isotopes of foreland basin sediments at Oytag (Wuyitake) in the Tarim Basin (west China): Journal of Asian Earth Sciences, v. 44, p. 136–148, https://doi.org/10.1016/j.jseaes.2011.04.020.

Black, L.P., Kamo, S.L., Allen, C.M., Davis, D.W., Aleinikoff, J.N., Valley, J.W., Mundil, R., Campbell, I.H., Korsch, R.J., Williams, I.S., and Foudoulis, C., 2004, Improved $^{206}Pb/^{238}U$ microprobe geochronology by the monitoring of a trace-element-related matrix effect; SHRIMP, ID-TIMS, ELA-ICP-MS and oxygen isotope documentation for a series of zircon standards: Chemical Geology, v. 205, p. 115–140, https://doi.org/10.1016/j.chemgeo.2004.01.003.

Blayney, T., Najman, Y., Dupont-Nivet, G., Carter, A., Millar, I., Garzanti., E., Sobel, E.R., Rittner, M., Andò, S., Guo, Z., and Vezzoli, G., 2016, Indentation of the Pamirs with respect to the northern margin of Tibet: Constraints from the Tarim basin sedimentary record: Tectonics, v. 35, p. 2345–2369, https://doi.org/10.1002/2016TC004222.

Blisniuk, P.M., and Stern, L.A., 2005, Stable isotope paleoaltimetry: A critical review: American Journal of Science, v. 305, p. 1033–1074, https://doi.org/10.2475/ajs.305.10.1033.

Bosboom, R., Dupont-Nivet, G., Grothe, A., Brinkhuis, H., Villa, G., Mandic, O., Stoica, M., Huang, W., Yang, W., Guo, Z., and Krijgsman, W., 2014, Linking Tarim Basin sea retreat (west China) and Asian aridification in the late Eocene: Basin Research, v. 26, p. 621–640, https://doi.org/10.1111/bre.12054.

Bougeois, L., Dupont-Nivet, G., de Rafélis, M., Tindall, J.C., Proust, J.N., Reichart, G.J., de Nooijer, L.J., Guo, Z., and Ormukov, C., 2018, Asian monsoons and aridification response to Paleogene sea retreat and Neogene westerly shielding indicated by seasonality in Paratethys oysters: Earth and Planetary Science Letters, v. 485, p. 99–110, https://doi.org/10.1016/j.epsl.2017.12.036.

Bullen, M.E., Burbank, D.W., Garver, J.I., and Abdrakhmatov, K.Y., 2001, Late Cenozoic tectonic evolution of the northwestern Tien Shan: New age estimates for the initiation of mountain building: Geological Society of America Bulletin, v. 113, no. 12, p. 1544–1559, https://doi.org/10.1130/0016-7606(2001)113<1544:LCTEOT>2.0.CO;2.

Carrapa, B., Mustapha, F.S., Cosca, M., Gehrels, G., Schoenbohm, L.M., Sobel, E.R., DeCelles, P.G., Russell, J., and Goodman, P., 2014, Multisystem dating of modern river detritus from Tajikistan and China: Implications for crustal evolution and exhumation of the Pamir: Lithosphere, v. 6, p. 443–455, https://doi.org/10.1130/L360.1.

Carrapa, B., DeCelles, P.G., Wang, X., Clementz, M.T., Mancin, N., Stoica, M., Kraatz, B., Meng, J., Abdulov, S., and Chen, F., 2015, Tectono-climatic implications of Eocene Paratethys regression in the Tajik basin of central Asia: Earth and Planetary Science Letters, v. 424, p. 168–178, https://doi.org/10.1016/j.epsl.2015.05.034.

Caves, J.K., Winnick, M.J., Graham, S.A., Sjostrom, D.J., Mulch, A., and Chamberlain, C.P., 2015, Role of the westerlies in Central Asia climate over the Cenozoic: Earth and Planetary Science Letters, v. 428, p. 33–43, https://doi.org/10.1016/j.epsl.2015.07.023.

Cerling, T.E., and Quade, J., 1993, Stable carbon and oxygen isotopes in soil carbonates, *in* Swart, P.K., Lohmann, K.C., McKenzie, J., and Savin, S. eds., Climate Change in Continental Isotopic Records: American Geophysical Union, Geophysical Monograph Series, v. 78, p. 217–231, https://doi.org/10.1029/GM078p0217.

Chang, J., Li, D., Min, K., Qiu, N., Xiao, Y., Wu, H., and Liu, N., 2019, Cenozoic deformation of the Kalpin fold-and-thrust belt, southern Chinese Tian Shan: New insights from low-T thermochronology and sandbox modeling: Tectonophysics, v. 766, p. 416–432, https://doi.org/10.1016/j.tecto.2019.06.018.

Charreau, J., Gilder, S., Chen, Y., Dominguez, S., Avouac, J.P., Sen, S., Jolivet, M., Li, Y., and Wang, W., 2006, Magnetostratigraphy of the Yaha section, Tarim Basin (China): 11 Ma acceleration in erosion and uplift of the Tian Shan mountains: Geology, v. 34, p. 181–184, https://doi.org/10.1130/G22106.1.

Charreau, J., Chen, Y., Gilder, S., Barrier, L., Dominguez, S., Augier, R., Sen, S., Avouac, J.-P., Gallaud, A., Graveleau, F., and Wang, Q., 2009, Neogene uplift of the Tian Shan Mountains observed in the magnetic record of the Jingou River section (northwest China): Tectonics, v. 28, https://doi.org/10.1029/2007TC002137.

Charreau, J., Kent-Corson, M.L., Barrier, L., Augier, R., Ritts, B.D., Chen, Y., France-Lannord, C., and Guilmette, C., 2012, A high-resolution stable isotopic record from the Junggar Basin (NW China): Implications for the paleotopographic evolution of the Tianshan Mountains: Earth and Planetary Science Letters, v. 341–344, p. 158–169, https://doi.org/10.1016/j.epsl.2012.05.033.

Chen, X., Chen, H., Cheng, X., Shen, Z., and Lin, X., 2015, Sedimentology and magnetostratigraphy of the Tierekesazi Cenozoic section in the foreland region of south West Tian Shan in Western China: Tectonophysics, v. 654, p. 156–172, https://doi.org/10.1016/j.tecto.2015.05.009.

Chen, X., Chen, H., Sobel, E.R., Lin, X., Cheng, X., Yan, J., and Yang, S., 2019, Convergence of the Pamir and the South Tian Shan in the late Cenozoic: Insights from provenance analysis in the Wuheshalu section at the convergence area: Lithosphere, v. 11, p. 507–523, https://doi.org/10.1130/L1028.1.

Cobbold, P.R., Sadybakasov, E., and Thomas, J.C., 1994, Cenozoic trans-pression and basin development, Kyrhjyz Tienshan, Central Asia, *in* Roure, F., Ellouz, N., Shein, V.S., and Skvortsov, I., eds., Geodynamic Evolution of Sedimentary Basins: International Symposium, Moscow, 18–23 May, p. 181–202.

Ducea, M.N. et al., 2003, Building the Pamirs: The view from the underside: Geology, v. 31, p. 849–852, https://doi.org/10.1130/G19707.1.

Dumitru, T.A., Zhou, D., Chang, E.Z., Graham, S.A., Hendrix, M.S., Sobel, E.R., and Carroll, A.R., 2001, Uplift, exhumation, and deformation in the Chinese Tian Shan, *in* Hendrix, M.S., and Davis, G.A., eds., Paleozoic and Mesozoic Tectonic Evolution of Central and Eastern Asia: From Continental Assembly to Intracontinental Deformation: Geological Society of America Memoir 194, p. 71–99, https://doi.org/10.1130/0-8137-1194-0.71.

Frisch, K., Voigt, S., Verestek, V., Appel, E., Albert, R., Gerdes, A., Arndt, I., Raddatz, J., Voigt, T., Weber, Y., and Batenburg, S.J., 2019, Long-period astronomical forcing of westerlies' strength in central Asia during Miocene climate cooling: Paleoceanography and Paleoclimatology, v. 34, p. 1784–1806, https://doi.org/10.1029/2019PA003642.

Graham, S.A., Chamberlain, C.P., Yue, Y., Ritts, B.D., Hanson, A.D., Horton, T.W., Waldbauer, J.R., Poage, M.A., and Feng, X., 2005, Stable isotope records of Cenozoic climate and topography, Tibetan plateau and Tarim basin: American Journal of Science, v. 305, p. 101–118, https://doi.org/10.2475/ajs.305.2.101.

Han, B.F., He, G.Q., Wang, X.C., and Guo, Z.J., 2011, Late Carboniferous collision between the Tarim and Kazakhstan-Yili terranes in the western segment of the South Tian Shan Orogen, Central Asia, and implications for the Northern Xinjiang, western China: Earth-Science Reviews, v. 109, p. 74–93, https://doi.org/10.1016/j.earscirev.2011.09.001.

Heermance, R.V., Chen, J., Burbank, W., and Wang, C., 2007, Chronology and tectonic controls of Late Tertiary deposition in the southwestern Tian Shan foreland, NW China: Basin Research, v. 19, p. 599–632 https://doi.org/10.1111/j.1365-2117.2007.00339.x.

Heermance, R.V., Chen, J., Burbank, D.W., and Miao, J., 2008, Temporal constraints and pulsed Late Cenozoic deformation during the structural disruption of the active Kashgar foreland, northwest China: Tectonics, v. 27, p. 1–27, https://doi.org/10.1029/2007TC002226.

Heermance, R.V., Pearson, J., Moe, A., Langtao, L., Jianhong, X., Jie, C., Richter, F., Garzione, C.N., Junsheng, N., and Bogue, S., 2018, Erg deposition and development of the ancestral Taklimakan Desert (western China) between 12.2 and 7.0 Ma: Geology, v. 46, p. 919–922, https://doi.org/10.1130/G45085.1.

Hubert-Ferrari, A., Suppe, J., Gonzalez-Mieres, R., and Wang, X., 2007, Mechanisms of active folding of the landscape (southern Tian Shan, China): Journal of Geophysical Research. Solid Earth, v. 112, p. 1–39, https://doi.org/10.1029/2006JB004362.

IAEA/WMO, 2020, Global Network of Isotopes in Precipitation: The GNIP Database, http://www.iaea.org/water.

Jepson, G., Glorie, S., Konopelko, D., Gillespie, J., Danišík, M., Evans, N.J., Mamadjanov, Y., and Collins, A.S., 2018, Thermochronological insights into the structural contact between the Tian Shan and Pamirs, Tajikistan: Terra Nova, v. 30, p. 95–104, https://doi.org/10.1111/ter.12313.

Jepson, G., Carrapa, B., Gillespie, J., Feng, R., DeCelles, P.G., Kapp, P., Tabor, C.R., and Zhu, J., 2021, Climate as the great equalizer of continental-scale erosion: Geophysical Research Letters, v. 48, p. 1–17, https://doi.org/10.1029/2021GL095008.

Jia, Y., Fu, B., Jolivet, M., and Zheng, S., 2015, Cenozoic tectono-geomorphological growth of the SW Chinese Tian Shan: Insight from AFT and detrital zircon U-Pb data: Journal of Asian Earth Sciences, v. 111, p. 395–413, https://doi.org/10.1016/j.jseaes.2015.06.023.

Jolivet, M., Dominguez, S., Charreau, J., Chen, Y., Li, Y., and Wang, Q., 2010, Mesozoic and Cenozoic tectonic history of the central Chinese Tian Shan: Reactivated tectonic structures and active deformation: Tectonics, v. 29, p. 1–30, https://doi.org/10.1029/2010TC002712.

Jolivet, M., Boulvais, P., Barrier, L., Robin, C., Heilbronn, G., Ledoyen, J., Ventroux, Q., Jia, Y., Guo, Z., and Bataleva, E.A., 2018, Oxygen and carbon stable isotope composition of cretaceous to Pliocene calcareous paleosols in the Tian Shan Region (Central Asia): Controlling factors and paleogeographic implications: Geosciences (Switzerland), v. 8, https://doi.org/10.3390/geosciences8090330.

Juhlke, T.R., Meier, C., van Geldern, R., Vanselow, K.A., Wernicke, J., Baidulloeva, J., Barth, J.A.C., and Weise, S.M., 2019, Assessing moisture sources of precipitation in the Western Pamir Mountains (Tajikistan, Central Asia) using deuterium excess: Tellus. Series B, Chemical and Physical Meteorology, v. 71, p. 1–16, https://doi.org/10.1080/16000889.2019.1601987.

Kent-Corson, M.L., Ritts, B.D., Zhuang, G., Bovet, P.M., Graham, S.A., and Page Chamberlain, C., 2009, Stable isotopic constraints on the tectonic, topographic, and climatic evolution of the northern margin of the Tibetan Plateau: Earth and Planetary Science Letters, v. 282, p. 158–166, https://doi.org/10.1016/j.epsl.2009.03.011.

Leng, M.J., and Marshall, J.D., 2004, Palaeoclimate interpretation of stable isotope data from lake sediment archives: Quaternary Science Reviews, v. 23, p. 811–831, https://doi.org/10.1016/j.quascirev.2003.06.012.

Li, L., and Garzione, C.N., 2017, Spatial distribution and controlling factors of stable isotopes in meteoric waters on the Tibetan Plateau: Implications for paleoelevation reconstruction: Earth and Planetary Science Letters, v. 460, p. 302–314, https://doi.org/10.1016/j.epsl.2016.11.046.

Li, L., Dupont-Nivet, G., Najman, Y., Kaya, M., Meijer, N., Poujol, M., and Aminov, J., 2022, Middle to late Miocene growth of the North Pamir: Basin Research, v. 34 p. 533–554, https://doi.org/10.1111/bre.12629.

Li, Q., Li, L., Zhang, Y., and Guo, Z., 2020, Oligocene incursion of the Paratethys seawater to the Junggar Basin, NW China: Insight from multiple isotopic analysis of carbonate: Scientific Reports, v. 10, p. 1–7, https://doi.org/10.1038/s41598-020-63609-0.

Li, S., Wang, X., and Suppe, J., 2012, Compressional salt tectonics and synkinematic strata of the western Kuqa foreland basin, southern Tian Shan, China: Basin Research, v. 24, p. 475–497, https://doi.org/10.1111/j.1365-2117.2011.00531.x.

Liu, L., Chen, J., and Li, T., 2017, Detrital zircon U-Pb dating of modern rivers' deposits in Pamir, South Tian Shan, and their convergence zone [in Chinese]: Dizhen Dizhi, v. 39, no. 3, p. 497–516.

Lü, L., Sun, J., Jia, Y., and Wu, L., 2021, Late Cenozoic thrust propagation within the Keping fold-and-thrust belt along the southern foreland of Chinese Tian Shan: Evidence from apatite (U-Th)/He results: Tectonophysics, v. 814, https://doi.org/10.1016/j.tecto.2021.228966.

Lukens, C.E., Carrapa, B., Singer, B.S., and Gehrels, G., 2012, Miocene exhumation of the Pamir revealed by detrital geothermochronology of Tajik rivers: Tectonics, v. 31, p. 1–12, https://doi.org/10.1029/2011TC003040.

Macaulay, E.A., Sobel, E.R., Mikolaichuk, A., Kohn, B., and Stuart, F.M., 2014, Cenozoic deformation and exhumation history of the Central Kyrgyz Tien Shan: Tectonics, v. 33, no. 2, p. 135–165, https://doi.org/10.1002/2013TC003376.

Macaulay, E.A., Sobel, E.R., Mikolaichuk, A., Wack, M., Gilder, S.A., Mulch, A., Fortuna, A.B., Hynek, S., and Apayarov, F., 2016, The sedimentary record of the Issyk Kul basin, Kyrgyzstan: Climatic and tectonic inferences: Basin Research, v. 28, p. 57–80, https://doi.org/10.1111/bre.12098.

Mattinson, J.M., 2010, Analysis of the relative decay constants of ^{235}U and ^{238}U by multi-step CA-TIMS measurements of closed-system natural zircon samples: Chemical Geology, v. 275, p. 186–198, https://doi.org/10.1016/j.chemgeo.2010.05.007.

McKnight, C.L., 1993, Structural styles and tectonic significance of Tian Shan foothill fold-thrust belts, northwest China [Ph.D. thesis]: Stanford, California, Stanford University, 207 p.

Mountney, N.P., 2012, A stratigraphic model to account for complexity in aeolian dune and interdune successions: Sedimentology, v. 59, p. 964–989, https://doi.org/10.1111/j.1365-3091.2011.01287.x.

Popov, S.V., Antipov, M.P., Zastrozhnov, A.S., Kurina, E.E., and Pinchuk, T.N., 2010, Sea-level fluctuations on the northern shelf of the Eastern Paratethys in the Oligocene-Neogene: Stratigraphy and Geological Correlation, v. 18, p. 200–224, https://doi.org/10.1134/S0869593810020073.

Qiao, Q., Huang, B., Piper, J.D.A., Deng, T., and Liu, C., 2016, Neogene magnetostratigraphy and rock magnetic study of the Kashgar Depression, NW China: Implications to neotectonics in the SW Tianshan Mountains Qingqing: Journal of Geophysical Research. Solid Earth, v. 121, p. 1280–1296, https://doi.org/10.1002/2015JB012687.

Qiao, Q., Huang, B., Biggin, A.J., and Piper, J.D.A., 2017, Late Cenozoic evolution in the Pamir-Tian Shan convergence: New chronological constraints from the magnetostratigraphic record of the southwestern Tianshan foreland basin (Ulugqat area): Tectonophysics, v. 717, p. 51–64, https://doi.org/10.1016/j.tecto.2017.07.013.

Quade, J.A.Y., and Roe, L.J., 1999, The stable-isotope composition of early ground-water cements from sandstone in paleoecological reconstruction: Journal of Sedimentary Research, v. 69, p. 667–674, https://doi.org/10.2110/jsr.69.667.

Rittner, M., Vermeesch, P., Carter, A., Bird, A., Stevens, T., Garzanti, E., Andò, S., Vezzoli, G., Dutt, R., Xu, Z., and Lu, H., 2016, The provenance of Taklamakan desert sand: Earth and Planetary Science Letters, v. 437, p. 127–137, https://doi.org/10.1016/j.epsl.2015.12.036.

Rowley, D.B., and Garzione, C.N., 2007, Stable isotope-based paleoaltimetry: Annual Review of Earth and Planetary Sciences, v. 35, p. 463–508, https://doi.org/10.1146/annurev.earth.35.031306.140155.

Sherfey, J.S., Soplata, A.E., Ardid, S., Roberts, E.A., Stanley, D.A., Pittman-Polletta, B.R., and Kopell, N.J., 2018, DynaSim: A MATLAB toolbox for neural modeling and simulation: Frontiers in Neuroinformatics, v. 12, p. 1–15, https://doi.org/10.3389/fninf.2018.00010.

Shi, Y., Sun, Z., and Qing, Y., 2008, Characteristics of area precipitation in Xinjiang region with its variations: Yingyong Qixiang Xuebao, v. 19, p. 326–332.

Sobel, E.R., and Dumitru, T.A., 1997, Thrusting and exhumation around the margins of the western Tarim basin during the India-Asia collision: Journal of Geophysical Research. Solid Earth, v. 102, p. 5043–5063, https://doi.org/10.1029/96JB03267.

Sobel, E.R., Chen, J., and Heermance, R.V., 2006, Late Oligocene-Early Miocene initiation of shortening in the Southwestern Chinese Tian Shan: Implications for Neogene shortening rate variations: Earth and Planetary Science Letters, v. 247, p. 70–81, https://doi.org/10.1016/j.epsl.2006.03.048.

Stacey, J.S., and Kramers, J.D., 1975, Approximation of terrestrial lead isotope evolution by a two-stage model: Earth and Planetary Science Letters, v. 26, p. 207–221, https://doi.org/10.1016/0012-821X(75)90088-6.

Sun, D., Bloemendal, J., Yi, Z., Zhu, Y., Wang, X., Zhang, Y., Li, Z., Wang, F., Han, F., and Zhang, Y., 2011, Palaeomagnetic and palaeoenvironmental study of two parallel sections of late Cenozoic strata in the central Taklimakan Desert: Implications for the desertification of the Tarim Basin: Palaeogeography, Palaeoclimatology, Palaeoecology, v. 300, p. 1–10, https://doi.org/10.1016/j.palaeo.2010.11.015.

Sun, J., and Liu, T., 2006, The age of the Taklimakan Desert: Science, v. 312, https://doi.org/10.1126/science.1124616.

Sun, J., Zhang, Z., and Zhang, L., 2009, New evidence on the age of the Taklimakan Desert: Geology, v. 37, p. 159–162, https://doi.org/10.1130/G25338A.1.

Sun, J., Liu, W., Liu, Z., Deng, T., Windley, B.F., and Fu, B., 2017, Extreme aridification since the beginning of the Pliocene in the Tarim Basin, western China: Palaeogeography, Palaeoclimatology, Palaeoecology, v. 485, p. 189–200, https://doi.org/10.1016/j.palaeo.2017.06.012.

Tera, F., and Wasserburg, G.J., 1972, U-Th-Pb systematics in lunar highland samples from the Luna 20 and Apollo 16 missions: Earth and Planetary Science Letters, v. 17, p. 36–51, https://doi.org/10.1016/0012-821X(72)90257-9.

Thompson, J.A., Burbank, D.W., Li, T., Chen, J., and Bookhagen, B., 2015, Late Miocene northward propagation of the northeast Pamir thrust system, northwest China: Tectonics, v. 34, p. 510–534, https://doi.org/10.1002/2014TC003690.

Thompson Jobe, J.A., Li, T., Bookhagen, B., Chen, J., and Burbank, D., 2018, Dating growth strata and basin fill by combining ^{26}Al/^{10}Be burial dating and magnetostratigraphy: Constraining active deformation in the Pamir-Tian Shan convergence zone, NW China: Lithosphere, v. 10, p. 806–828, https://doi.org/10.1130/L727.1.

Tian, L., Yao, T., MacClune, K., White, J.W.C., Schilla, A., Vaughn, B., Vachon, R., and Ichiyanagi, K., 2007, Stable isotopic variations in west China: A consideration of moisture sources: Journal of Geophysical Research, D, Atmospheres, v. 112, p. 1–12, https://doi.org/10.1029/2006JD007718.

Turner, S.A., Cosgrove, J.W., and Liu, J.G., 2010, Controls on lateral structural variability along the Keping Shan Thrust Belt, SW Tien Shan Foreland, China, *in* Goffey, G.P., Craig, J., Needham, T., and Scott, R., eds., Hydrocarbons in Contractional Belts: Geological Society Special Publication, v. 348, p. 71–85, https://doi.org/10.1144/SP348.5.

Vergés, J., Marzo, M., and Muñoz, J.A., 2002, Growth strata in foreland settings: Sedimentary Geology, v. 146, p. 1–9, https://doi.org/10.1016/S0037-0738(01)00162-2.

Vermeesch, P., 2018, IsoplotR: A free and open toolbox for geochronology: Geoscience Frontiers, v. 9, p. 1479–1493, https://doi.org/10.1016/j.gsf.2018.04.001.

Vermeesch, P., 2021, On the treatment of discordant detrital zircon U-Pb data: Geochronology, v. 3, p. 247–257, https://doi.org/10.5194/gchron-3-247-2021.

Vilkas, M., 2019, Detrital zircon geochronology of the Southern Tian Shan Foreland and implications for Late Cenozoic tectonics of regional intracontinental orogenic systems, northwestern China: Northridge, USA, California State University, Department of Geological Sciences, p. 1–98, http://hdl.handle.net/10211.3/207799.

Wang, S., Zhang, M., Che, Y., Zhu, X., and Liu, X., 2016a, Influence of below-cloud evaporation on deuterium excess in precipitation of arid Central Asia and its meteorological controls: Journal of Hydrometeorology, v. 17, p. 1973–1984, https://doi.org/10.1175/JHM-D-15-0203.1.

Wang, S., Zhang, M., Hughes, C.E., Zhu, X., Dong, L., Ren, Z., and Chen, F., 2016b, Factors controlling stable isotope composition of precipitation in arid conditions: An observation network in the Tianshan Mountains, central Asia: Tellus. Series B, Chemical and Physical Meteorology, v. 68, https://doi.org/10.3402/tellusb.v68.26206.

Wang, S., Zhang, M., Crawford, J., Hughes, C.E., Du, M., and Liu, X., 2017, The effect of moisture source and synoptic conditions on precipitation isotopes in arid central Asia: Journal of Geophysical Research. Atmospheres, v. 122, p. 2667–2682, https://doi.org/10.1002/2015JD024626.

Wang, X., Sun, D., Chen, F., Wang, F., Li, B., Popov, S.V., Wu, S., Zhang, Y., and Li, Z., 2014, Cenozoic paleo-environmental evolution of the Pamir-Tien Shan convergence zone: Journal of Asian Earth Sciences, v. 80, p. 84–100, https://doi.org/10.1016/j.jseaes.2013.10.027.

Wang, X., Carrapa, B., Chapman, J.B., Henriquez, S., Wang, M., DeCelles, P.G., Li, Z., Wang, F., Oimuhammadzoda, I., Gadoev, M., and Chen, F., 2019, Parathethys last gasp in central Asia and late Oligocene accelerated uplift of the Pamirs: Geophysical Research Letters, v. 46, p. 11,773–11,781, https://doi.org/10.1029/2019GL084838.

Wang, X., Carrapa, B., Sun, Y., Dettman, D.L., Chapman, J.B., Caves Rugenstein, J.K., Clementz, M.T., DeCelles, P.G., Wang, M., Chen, J., Quade, J., Wang, F., Li, Z., Oimuhammadzoda, I., Gadoev, M., Lohmann, G., Zhang, X., and Chen, F., 2020, The role of the westerlies and orography in Asian hydroclimate since the late Oligocene: Geology, v. 48, p. 728–732, https://doi.org/10.1130/G47400.1.

Westerhold, T., Marwan, N., Drury, A.J., Liebrand, D., Agnini, C., Anagnostou, E., Barnet, J.S.K., Bohaty, S.M., De Vleeschouwer, D., Florindo, F., Frederichs, T., Hodell, D.A., Holbourn, A.E., Kroon, D., Lauretano, V., Littler, K., Lourens, L.J., Lyle, M., Pälike, H., Röhl, U., Tian, J., Wilkens, R.H., Wilson, P., and Zachos, J.C., 2020, An astronomically dated record of Earth's climate and its predictability over the last 66 million years: Science, v. 369, p. 1383–1387, https://doi.org/10.1126/science.aba6853.

Wiedenbeck, M., Allé, P., Corfu, F., Griffin, W.L., Meier, M., Oberli, F., Von Quadt, A., Roddick, J.C., and Spiegel, W., 1995, Three natural zircon standards for U-Th-Pb, Lu-Hf trace element and REE analyses: Geostandards Newsletter, v. 19, p. 1–23, https://doi.org/10.1111/j.1751-908X.1995.tb00147.x.

Wright, P., and Tucker, M.E., 1991, Calcretes: An introduction, *in* Wright, P., and Tucker, M.E., eds., Calcretes: The International Association of Sedimentologists: Oxford, UK, Blackwell Scientific Publications, v. 2, p. 1–22, https://doi.org/10.1002/9781444304497.ch.

Yang, Y., Yao, W.-Q., Yan, J.-J., Guo, Y., and Xie, D.-Q., 2018, Mesozoic and Cenozoic structural deformation in the NW Tarim Basin, China: A case study of the Piqiang-Selibuya Fault: International Geology Review, v. 60, no. 7, p. 929–943, https://doi.org/10.1080/00206814.2017.1360803.

Yin, A., Nie, S., Craig, P., Harrison, T.M., Ryerson, F.J., Xianglin, Q., and Geng, Y., 1998, Late Cenozoic tectonic evolution of the southern Chinese Tian Shan: Tectonics, v. 17, no. 1, p. 1–27, https://doi.org/10.1029/97TC03140.

Zachos, J., Pagani, H., Sloan, L., Thomas, E., and Billups, K., 2001, Trends, rhythms, and aberrations in global climate 65 Ma to present: Science, v. 292, p. 686–693, https://doi.org/10.1126/science.1059412.

Zhang, T., Fang, X., Song, C., Appel, E., and Wang, Y., 2014, Cenozoic tectonic deformation and uplift of the South Tian Shan: Implications from magnetostratigraphy and balanced cross-section restoration of the Kuqa depression: Tectonophysics, v. 628, p. 172–187, https://doi.org/10.1016/j.tecto.2014.04.044.

Zhang, Y., Yang, S., Chen, H., Dilek, Y., Cheng, X., Lin, X., Wang, C., and Zhu, T., 2019, The effect of overburden thickness on deformation mechanisms in the Keping fold-thrust belt, southwestern Chinese Tian Shan Mountains: Insights from analogue modeling: Tectonophysics, v. 753, p. 79–92, https://doi.org/10.1016/j.tecto.2019.01.005.

Zheng, H., Wei, X., Tada, R., Clift, P.D., Wang, B., Jourdan, F., Wang, P., and He, M., 2015, Late Oligocene-early Miocene birth of the Taklimakan Desert: Proceedings of the National Academy of Sciences of the United States of America, v. 112, p. 7662–7667, https://doi.org/10.1073/pnas.1424487112.

Zhuang, G., Hourigan, J.K., Koch, P.L., Ritts, B.D., and Kent-Corson, M.L., 2011, Isotopic constraints on intensified aridity in Central Asia around 12 Ma: Earth and Planetary Science Letters, v. 312, p. 152–163, https://doi.org/10.1016/j.epsl.2011.10.005.

Science Editor: Mihai Ducea
Associate Editor: Galen Halverson

Manuscript Received 25 January 2022
Revised Manuscript Received 17 June 2022
Manuscript Accepted 23 July 2022

Printed in the USA